A counterclockwise *PTt* path of high-pressure/low-temperature rocks from the Coastal Cordillera accretionary complex of south-central Chile: constraints for the earliest stage of subduction mass flow

A.P. Willner[a,*], J. Glodny[b], T.V. Gerya[a,c], E. Godoy[d], H.-J. Massonne[e]

[a] *Institut für Geologie, Mineralogie und Geophysik, Ruhr-Universität Bochum, Universitätsstrasse 150, D-44780 Bochum, Germany*
[b] *GeoForschungsZentrum Potsdam, Telegrafenberg C2, D-14473 Potsdam, Germany*
[c] *Institute of Experimental Mineralogy, Russian Academy of Sciences, Chernogolovka, Moskow District 142432, Russia*
[d] *Servicio Nacional de Geología y Minería, Casilla 10465, Santiago, Chile*
[e] *Institut für Mineralogie und Kristallchemie, Universität Stuttgart, Azenbergstr. 18, D-70174 Stuttgart, Germany*

Abstract

Within the metamorphic basement of the Coastal Cordillera of central Chile, the Western Series constitutes the high-pressure (HP)/low-temperature (LT) part (accretionary prism) of a fossil-paired metamorphic belt dominated by metagreywackes. In its eastern part, blocks derived from small lenses of garnet amphibolite with a blueschist facies overprint are locally intercalated and associated with serpentinite and garnet mica-schist. Continuously developed local equilibria were evaluated applying various independent geothermobarometric approaches. An overall anticlockwise *PT* path results. The prograde path evolved along a geothermal gradient of ~ 15 °C/km, passing the high-pressure end of greenschist facies until a transient assemblage developed within albite-epidote amphibolite facies transitional to eclogite facies at peak metamorphic conditions (600–760 °C, 11–16.5 kbar; stage I). This peak assemblage was overprinted during an external fluid infiltration by an epidote blueschist facies assemblage at 350–500 °C, 10–14 kbar (stage II) indicating nearly isobaric cooling. The retrograde equilibration stage was dated with a Rb–Sr mineral isochron at 305.3 ± 3.2 Ma, somewhat younger (296.6 ± 4.7 Ma) in an adjacent garnet mica-schist. Localized retrograde equilibration continued during decompression down to ~ 300 °C, 5 kbar. The retrograde evolution is identical in the garnet amphibolite and the garnet mica-schist.

The counterclockwise *PT* path contrasts the usual clockwise *PT* paths derived from rocks of the Western Series. In addition, their ages related to stage II are the oldest recorded within the fossil wedge at the given latitude. Its "exotic" occurrence is interpreted by the path of the earliest and deepest subducted material that was heated in contact with a still hot mantle. Later accreted and dehydrated material caused hydration and cooling of the earliest accreted material and the neighbouring mantle. After this change also related to rheological conditions, effective exhumation of the early subducted material followed at the base of the hydrated mantle wedge within a cooler environment (geothermal gradient around 10–15 °C/km) than during its burial. The exotic blocks thus provide important time markers for the onset of subduction mass circulation in the Coastal

* Corresponding author. Fax: +49-234-32-14433.
E-mail address: arne.willner@ruhr-uni-bochum.de (A.P. Willner).

Cordillera accretionary prism during the Late Carboniferous. Continuous subduction mass flow lasted for nearly 100 Ma until the Late Triassic.

1. Introduction

Critical for the understanding of the evolution of subduction zones is the study of sets of interrelated *PT* paths from exhumed high-pressure (HP) metamorphic complexes that can also directly be compared with numerical modelling results (e.g. Peacock, 1990; Guinchi and Ricard, 1999; Gerya et al., 2002). Although in HP–low-temperature (LT) rocks of fossil accretionary prisms generally clockwise partial *PT* paths are recorded (e.g. Maruyama and Liou, 1988; Massonne, 1995a,b), increasing evidence of counterclockwise *PT* paths in locally restricted occurrences became available within this type of geotectonic regime during the past decade (Wakabayashi, 1990; Oh and Liou, 1990; Krogh et al., 1994; Perchuk et al., 1999; Smith et al., 1999; Krebs et al., 2001). Such examples were recorded from relatively small-scale tectonic blocks (e.g. in the Franciscan: Wakabayashi, 1990; Oh and Liou, 1990), which also differ from the regional surrounding HP–LT rocks by generally showing higher peak *PT* conditions and older ages of metamorphism. The presence of such isolated "exotic" blocks with their systematic characteristics seems to be a typical feature for deeply eroded accretionary prisms that must be explained by more refined geodynamic models.

In this paper, we report on glaucophane-bearing garnet amphibolite of Los Pabilos, a so far unique example of a tectonic body with a counterclockwise *PT* path from the metamorphic basement in the Chilean Coastal Cordillera (Fig. 1). This basement constitutes a very long trending chain of fossil accretionary prisms, between about 30 and 54°S (Forsythe, 1982; Hervé, 1988; Fig. 1). For the main volume of rocks of these accretionary prisms, the widespread occurrence of phengite in metapsammopelites and metabasites (e.g. Massonne et al., 1996) and quantitative geothermobarometric studies (Willner et al.,

2000, 2001) point to preserved peak metamorphic conditions of a low *PT* gradient, with metamorphic conditions transitional from greenschist to blueschist facies, typical for subduction regimes. Traditionally, the HP–LT nature of the rocks was inferred only by reports of local glaucophane-bearing rocks at Pichilemu (34°30′S) by Aguirre et al. (1972) and at Los Pabilos (40°57′S) by Kato (1985). Thus, HP–LT rocks were believed to be rare along the convergent continental margin of South America a decade ago.

The glaucophane-bearing garnet amphibolite of Los Pabilos was first described by Kato (1985) and the field relationships were presented in detail by Kato and Godoy (1995), who also mentioned rare relics of omphacite. The scope of our study is to derive a quantitative *PT*–time (*t*) path for this rock type, in order to provide an important constraint for refined conceptual models of mass transport in deep-rooted accretionary wedges.

2. Geological setting

The Chilean Coastal Cordillera accretionary complexes generally consist of two major units (Aguirre et al., 1972; Hervé, 1988; Willner et al., 2000; Fig. 1): The low-grade (transitional greenschist- to blueschist facies) Western Series contains rocks of continental provenance (metagreywacke and metapelite; ~ 80–85%) and oceanic origin (metabasite; serpentinite; metachert; meta-exhalites; ~ 15–20%) and is characterized by a penetrative flat transposition foliation. The very low-grade and less-deformed Eastern Series contains metagreywackes with well-preserved sedimentary structures, corresponding to a turbiditic environment, and with stratigraphic continuity at outcrop scale. Between 34 and 40°S, the Eastern Series was intruded by a late Paleozoic calc-alkaline batholith and locally overprinted by a low-pressure
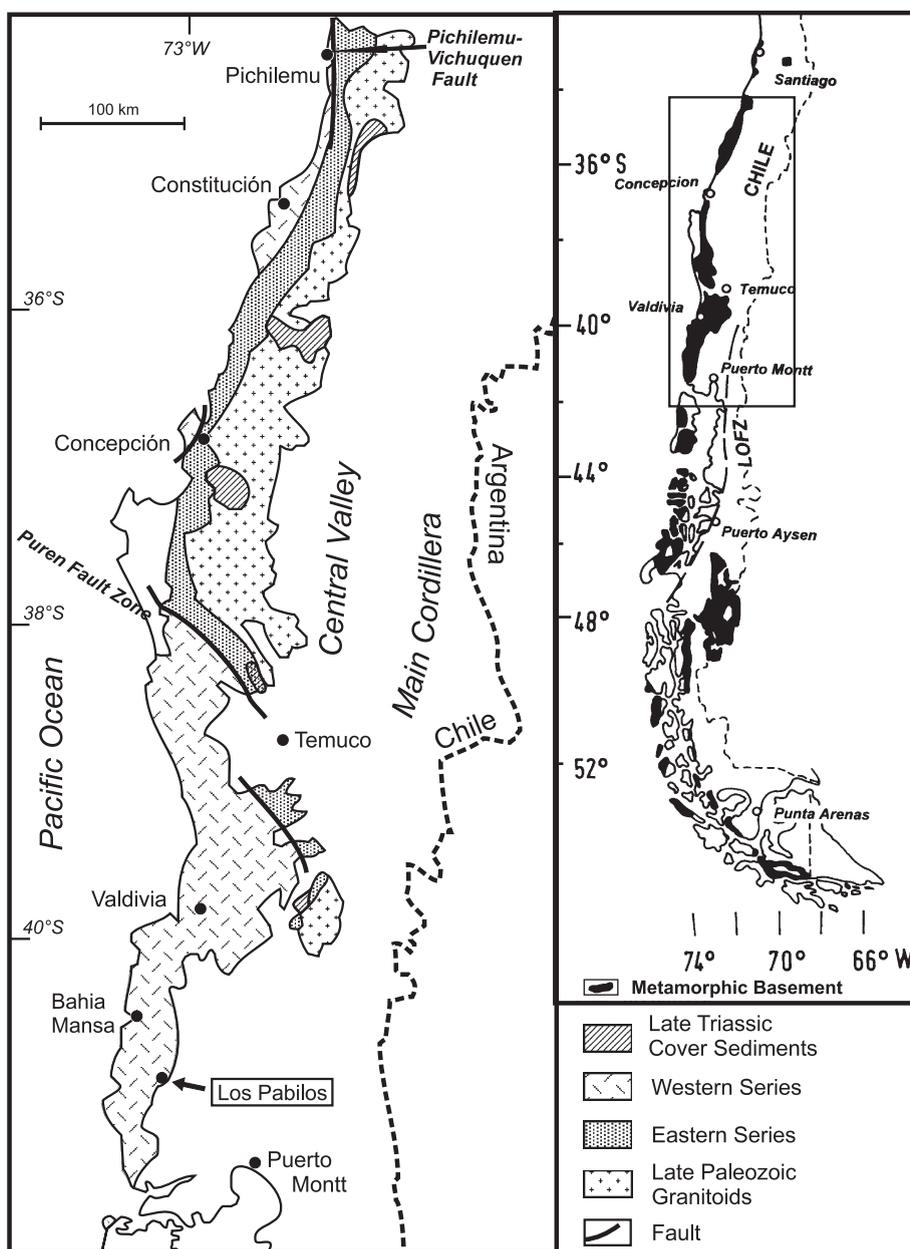
Fig. 1. Geological map of the basement of the Chilean Coastal Cordillera between 34° and 42°S.

(LP)–high-temperature (HT) metamorphism. This setting was interpreted by Aguirre et al. (1972) as a paired metamorphic belt. Further south in the Chonos Archipelago (44–47°S), Willner et al. (2000) showed that rocks, previously assigned to those series, but with partly Triassic protolith ages, were metamorphosed (at peak conditions) under a common metamorphic gradient of 12–13 °C/km. These authors suggested that the Eastern Series represents a higher level of the accretionary wedge preserved in the retrowedge zone transitional to the back stop system.

In the Coastal Cordillera of south-central Chile, between 39°30′ and 42°00′S, exposures of the Western Series prevail. They represent the framework of our study locality (Fig. 1). Metapsammopelites predominate with about 20% of metabasic intercalations. A clockwise *PT* path, probably typical for this region, was derived by Willner et al. (2001) with peak *PT* conditions of 300–370 °C and 6–8 kbar and a retrograde path characterized by decompression to 2 kbar and cooling to temperatures somewhat below 300 °C, external fluid influx, and strain-free crystallisation of retrograde phases. The widespread occurrence of stilpnomelane + potassic white mica (for *PT* stability, see Massonne and Szpurka, 1997) in this basement segment (González-Bonorino, 1970; Kato, 1985) suggests similar *PT* conditions below 350–400 °C. Nevertheless, local occurrences of metapelites with the assemblage biotite + potassic white mica and of garnet-bearing metabasites (Kato, 1985) point to local higher maximum temperatures (and presumably pressures). From maps showing corresponding mineral assemblages, no clear regional zonation trend is discernible. However, the regional structural trend is consistently NW–SE with a predominant, mostly flat lying, s_2 foliation transposing earlier structures such as sedimentary features and relict s_1 planes. The s_2 foliation is parallel to the axial plane of recumbent cm- to m-scale F_2 folds. Fold axes and stretching lineations are parallel to the general NW–SE trend. The s_2 foliation, which was refolded by large-scale open F_3 folds, is here considered a basal accretion feature formed during the early retrograde *PT* path by ductile thinning (Willner et al., 2000, 2001).

The glaucophane-bearing garnet amphibolite of Los Pabilos occurs within a poorly exposed region of the Western Series characterized by an intensively weathered surface covered by dense forests. Although a thorough account of the local geological situation was presented in Kato and Godoy (1995), the geological relationships of these exceptional rocks still remain unclear. The garnet amphibolite is present at two localities of several 100-m extent as loose boulders of mostly dm-size locally concentrated on top of an erosional plateau. The rocks of the immediately surrounding areas are interfoliated greenschist, serpentinite and quartz mica-schist typical for the Western Series. The occurrence of some serpentinite boulders together with those of the garnet amphibolite at one

(Cuesta Brava; 73°46.75′W/40°57,91′S) of the two localities suggested to Kato and Godoy (1995) a close relationship with a nearby occurrence of a serpentinite lens striking parallel to the regional WNW–ESE trending penetrative foliation. Thus, the garnet amphibolite boulders might represent autochthonous weathering relics of a lens associated to the serpentinite body. We collected several samples from the Cuesta Brava locality including a boulder of garnet mica-schist.

Chemical analyses of the Los Pabilos garnet amphibolite by Kato and Godoy (1995) revealed mid-oceanic-ridge basalt signatures with a tendency to primitive island arc composition, similar to other metabasites of the surrounding Western Series. For the garnet amphibolite of Los Pabilos, a K–Ar age of white mica of 304 ± 9 Ma (Kato and Godoy, 1995) and an Ar–Ar age of white mica of 323 ± 2 Ma (Kato et al., 1997) are mentioned. These values differ from other age data so far measured for the Western Series between 39.5 and 42°S. Glodny et al. (2002a) reported Rb–Sr mineral isochron age data for the main penetrative deformation of the country rocks, in the range between ∼ 250 and ∼ 230 Ma, with a trend of younging towards the south. Duhart et al. (2001) summarize Ar–Ar and K–Ar ages of potassic white mica in this area, regarded as cooling ages, which cover a wide range clustering between ∼ 270 and ∼ 215 Ma. Martin et al. (1999) suggested that peak (high *P/T*) metamorphism within the Western Series occurred between 328 and 304 Ma, and was followed by a nearly complete retrogression at <275 Ma. In this paper, we oppose this view. Instead, we intend to show that the garnet amphibolite of Los Pabilos is far more "exotic" than previously thought, being part of a tectonic body with a *PTt* evolution completely different from the main volume of the Western Series rocks in the area. While a Late Carboniferous metamorphic age was suggested for the Los Pabilos garnet amphibolites, the main volume of material was not even subducted at that time: Duhart et al. (2001) presented spectra of U–Pb single grain ages for detrital zircon from metapsammopelitic schists of the Western Series rocks sampled between 39.5 and 42°S. Several concordant detritus ages younger than 300 Ma (down to 275 Ma) are a priori in conflict with the above inferred Late Carboniferous HP metamorphic stage. Duhart et al. (2001) invoked "at least two episodes of deposition and a similar

number of deformation and metamorphic events'' to explain this discrepancy. Instead, we propose that continuous subduction mass flow circulation over a certain time seems to be more conceivable.

Granites that intruded the Eastern Series at the same latitudes yielded U–Pb ages of 282–306 Ma (Martin et al., 1999). The oldest sediments, which unconformably overlie the basement rocks, are continental siliciclastic rocks of Late Triassic age (Martin et al., 1999). The major sinistral NW–SE trending Puren fault zone ($37°40′−39°20′S$) juxtaposed the Western Series and the continuation of the Permo-Carboniferous magmatic arc to the north and may have controlled Triassic sedimentation (Echtler et al., 2003; Fig. 1). Exhumation of the Western Series, related to basal accretionary processes, continued to the Late Triassic (Glodny et al., 2002a). If this view is correct, the entire accretionary mass flow, with partly concomitant magmatic arc activity, was active between Late Carboniferous and Late Triassic times for the section of the Chilean Coastal Cordillera considered here.

3. Analytical methods

Mineral analyses were achieved with a Cameca SX 50 microprobe at Ruhr-Universität Bochum, Germany. Operating conditions were an acceleration voltage of 15 kV, a beam current of 15 nA, 20 s counting time per element on the peak and on the background and a defocussed beam of 8 μm diameter in order to avoid loss of alkalies in micas, feldspars and amphiboles. Standards used were synthetic pyrope (Si, Al, Mg), rutile (Ti), glass of andradite composition (Ca, Fe), jadeite (Na), K-bearing glass (K), topaz (F), Ba-silicate glass (Ba; Lα). The PAP procedure was used for matrix correction. Representative analyses and structural formulae of minerals used for *PT* calculations, together with the calculation procedure of the structural formulae, are presented in Table 1. Further analyses may be provided upon request to the first author. Element distribution maps were simultaneously produced for three elements by stepwise scanning over rectangular areas using a Camebax microprobe in Bochum. Abbreviations for minerals and mineral components used throughout the text are in line with

Kretz (1983). Abbreviations not included in Kretz (1983) are: Kwm—K-white mica, Nam—Na-amphibole, Cam—Ca-amphibole and V—vapour.

Mineral concentrates of two samples, a garnet amphibolite and a garnet mica-schist, were analyzed for their Rb–Sr mineral systematics by isotope dilution methods. Mass spectrometric analysis was done at the GFZ Potsdam. Analytical procedures are presented in detail by Glodny et al. (2002b).

4. Petrographical characteristics and mineral chemistry

4.1. Garnet amphibolite

The principal rock type of the exotic blocks of Los Pabilos is a garnet amphibolite (samples 96CH-143, -144, -145, -161) dominated by coarse amphibole (0.4–2.0 mm), garnet (1–3 mm), epidote (0.3–1.0 mm) with interstitial chlorite (0.1–0.5 mm), white mica (0.1–0.5 mm), rutile, titanite and/or ilmenite. In some cases, amphibole and epidote reveal a certain orientation. The amphibolite boulders may lack garnet, sharing, however, similar features with the garnet-bearing ones. The principal fabric shows clear evidence of two distinctly different superimposed metamorphic assemblages (Fig. 2). The mineral characteristics presented in the following correspond well with features already observed by Kato and Godoy (1995).

Amphibole reveals most diversity of composition and fabric. A first amphibole generation (Am 1; Table 1) is represented by rare relics with high Na-contents enclosed in garnet. These amphiboles are winchite (Na^B on the octahedral site ~ 0.8 per formula unit, pfu) or actinolite (Na^B ~ 0.48 pfu; Am 1a) and actinolitic hornblende within hornblende (Am 1b; Na^B ~ 0.8 pfu with elevated Na^A on the A-site ~ 0.2 pfu). Most prominently, the predominant amphibole crystals of the matrix have dark green cores and 0.1–0.5 mm wide blue rims with clear discontinuous boundaries. All degrees of reaction, between incipient formation of blue amphibole and a nearly complete replacement of green by blue amphibole, can be observed in different samples. The green cores (Am 2) are partly intergrown with potassic white mica and chlorite along rational grain boundaries or they

Table 1
Representative analyses of minerals

Amphibole	96CH143						96CH144			96CH145		
	Am 1a	Am 1b	Am 2 core	Am 2 rim	Am 3	Am 4	Am 2	Am 3	Am 4	Am 1a	Am 2	Am 3
SiO_2	54.64	50.91	41.29	42.03	55.78	53.65	43.90	56.37	53.52	52.61	41.34	55.97
TiO_2	0.05	0.27	1.19	1.04	0.08	0.03	0.96	0.04	0.00	0.03	1.28	0.02
Al_2O_3	4.73	6.50	14.11	13.79	9.95	1.98	13.29	11.47	1.32	3.14	14.04	9.87
Fe_2O_3[a]	3.01	1.30	2.91	2.46	2.99	4.59	1.89	2.55	1.57	4.93	2.64	2.79
FeO	10.12	13.07	15.30	15.98	10.42	9.85	11.56	8.60	14.22	13.06	15.40	13.25
MnO	0.22	0.24	0.19	0.29	0.16	0.35	0.08	0.05	0.45	0.10	0.10	0.08
MgO	13.32	12.44	7.97	7.65	9.36	15.20	11.13	9.80	13.45	12.35	8.08	7.12
CaO	7.66	10.30	9.59	9.26	1.74	10.92	10.36	1.30	11.75	9.81	9.60	0.81
Na_2O	3.28	2.11	3.46	3.61	6.74	1.45	3.37	0.11	0.65	1.95	3.75	6.87
K_2O	0.06	0.44	1.25	1.27	0.03	0.09	0.29	6.71	0.05	0.10	0.84	0.03
H_2O[a]	2.10	2.06	1.98	1.98	2.14	2.09	2.03	2.16	2.04	2.06	1.98	2.10
Sum	99.19	99.64	99.24	99.36	99.39	100.20	98.86	99.16	99.02	100.14	99.05	98.91
Si	7.805	7.401	6.253	6.360	7.831	7.694	6.483	7.823	7.854	7.645	6.261	7.953
Al^{IV}	0.195	0.599	1.747	1.640	0.169	0.306	1.517	0.177	0.146	0.355	1.739	0.047
Ti	0.005	0.029	0.135	0.118	0.008	0.003	0.107	0.004	0.000	0.004	0.146	0.002
Al^{VI}	0.601	0.514	0.772	0.819	1.477	0.029	0.795	1.700	0.827	0.184	0.767	1.605
Fe^{3+}	0.324	0.142	0.332	0.280	0.316	0.496	0.210	0.266	0.174	0.539	0.301	0.299
Fe^{2+}	1.209	1.589	1.937	2.021	1.223	1.181	1.428	0.998	1.746	1.587	1.950	1.575
Mn	0.027	0.030	0.024	0.037	0.019	0.042	0.010	0.006	0.056	0.013	0.012	0.010
Mg	2.835	2.696	1.799	1.725	1.958	3.249	2.450	2.027	2.942	2.674	1.823	1.509
Ca	1.172	1.604	1.556	1.502	0.261	1.678	1.640	0.193	1.847	1.528	1.558	0.123
Na	0.907	0.594	1.017	1.058	1.833	0.403	0.964	1.806	0.185	0.550	1.101	1.893
K	0.011	0.082	0.242	0.245	0.005	0.017	0.055	0.005	0.009	0.019	0.162	0.000
OH	2.000	2.000	2.000	2.000	2.000	2.000	2.000	2.000	2.000	2.000	2.000	2.000
X_{Mg}	0.696	0.625	0.478	0.456	0.612	0.726	0.630	0.669	0.620	0.626	0.482	0.488
$X_{Fe^{3+}}$	0.350	0.216	0.300	0.255	0.176	0.945	0.209	0.135	0.678	0.746	0.282	0.157

Cations based on 46 valencies and sum of cations = 13 except for Ca, Na and K for estimation of Fe^{3+}.

White mica	Garnet amphibolite						Garnet mica-schist
	96CH143		96CH144		96CH145		96CH156
	Inclusion	Matrix	Inclusion	Matrix	Inclusion	Matrix	
SiO_2	47.51	50.07	48.72	49.98	48.52	49.15	50.13
TiO_2	0.27	0.15	0.07	0.20	0.08	0.21	0.16
Al_2O_3	23.21	24.16	26.66	26.85	26.62	26.03	27.68
FeO	7.70	4.57	3.45	2.17	5.01	4.68	3.73
MnO	0.17	0.05	0.00	0.07	0.02	0.04	0.02
MgO	3.19	3.49	2.86	3.16	2.51	2.69	2.28
CaO	0.06	0.02	0.02	0.00	0.00	0.00	0.00
BaO	0.12	n.d.	0.35	0.14	0.27	0.46	n.d.
Na_2O	0.07	0.11	0.15	0.51	0.30	0.29	0.39
K_2O	10.57	11.19	10.74	10.70	10.91	10.77	10.20
H_2O[b]	4.28	4.50	4.34	4.40	4.36	4.36	4.44
Sum	97.15	98.31	97.36	98.18	98.60	98.68	99.03
Si	6.654	6.906	6.739	6.801	6.680	6.765	6.749
Al^{IV}	1.347	1.094	1.261	1.199	1.320	1.236	1.251
Al^{VI}	2.484	2.834	3.085	3.107	2.998	2.987	3.140
Ti	0.029	0.016	0.007	0.002	0.008	0.021	0.016

Table 1 (*continued*)

White mica	Garnet amphibolite						Garnet mica-schist
	96CH143		96CH144		96CH145		96CH156
	Inclusion	Matrix	Inclusion	Matrix	Inclusion	Matrix	
Fe^{2+}	0.311	0.501	0.399	0.247	0.486	0.538	0.420
Fe^{3+}	0.590	0.026	0.000	0.000	0.091	0.000	0.000
Mn	0.020	0.006	0.000	0.007	0.003	0.005	0.002
Mg	0.666	0.718	0.591	0.641	0.514	0.552	0.457
Ca	0.009	0.003	0.003	0.000	0.000	0.000	0.000
Ba	0.006	n.d.	0.019	0.007	0.014	0.025	n.d.
Na	0.019	0.029	0.040	0.135	0.079	0.077	0.102
K	1.888	1.969	1.895	1.857	1.916	1.890	1.752
OH	4.000	4.000	4.000	4.000	4.000	4.000	4.000
X_{Ms}	0.435	0.465	0.544	0.501	0.530	0.492	0.529
X_{MAC}	0.228	0.268	0.227	0.292	0.179	0.200	0.199
X_{FAC}	0.107	0.187	0.153	0.113	0.169	0.195	0.183
X_{Mg}	0.681	0.588	0.596	0.721	0.514	0.506	0.521

The amounts of cations are based on 42 valencies neglecting the interlayer cations. The sum of octahedrally coordinated cations is set to 4.1 to allow for an estimation of Fe^{3+}. The amounts of Cr, Cl and F are near or below detection limit. Symbols: Ms = muscovite, MAC = Mg-Al-celadonite and FAC = Fe-Al-celadonite.

Garnet	Garnet amphibolite						Garnet mica-schist	
	96CH143		96CH144		96CH145		96CH156	
	Core	Rim	Core	Rim	Core	Rim	Core	Rim
SiO_2	37.86	37.78	37.69	38.05	37.48	37.84	36.50	36.32
TiO_2	0.04	0.04	0.04	0.06	0.17	0.06	0.12	0.09
Al_2O_3	20.67	20.84	21.13	21.45	20.56	20.98	20.70	20.44
FeO	21.79	23.42	23.71	23.67	22.84	23.66	19.93	23.43
$Fe_2O_3^c$	1.08	1.41	0.68	0.41	1.16	0.64	1.13	1.41
MnO	7.67	3.42	3.24	2.51	2.95	2.37	10.62	6.81
MgO	3.05	3.61	2.72	3.16	3.22	3.22	0.23	0.32
CaO	7.84	9.64	10.58	10.86	10.49	10.51	10.65	10.65
Sum	100.00	100.16	99.79	100.17	98.87	99.28	99.88	99.47
Si	6.010	5.957	5.971	5.975	5.977	5.997	5.897	5.895
Al^{IV}	0.000	0.043	0.029	0.025	0.023	0.003	0.103	0.105
Al^{VI}	3.866	3.829	3.915	3.946	3.841	3.916	3.844	3.804
Fe^{3+}	0.130	0.167	0.081	0.048	0.139	0.077	0.140	0.185
Ti	0.004	0.005	0.004	0.007	0.020	0.007	0.016	0.011
Mg	0.721	0.847	0.642	0.740	0.767	0.760	0.054	0.079
Fe^{2+}	2.893	3.088	3.141	3.109	3.046	3.135	2.693	3.181
Mn	1.031	0.457	0.434	0.334	0.398	0.318	1.454	0.886
Ca	1.334	1.628	1.796	1.827	1.792	1.784	1.843	1.796
X_{And}	0.007	0.011	0.006	0.004	0.010	0.006	0.011	0.014
X_{Sps}	0.172	0.076	0.072	0.056	0.066	0.053	0.241	0.155
X_{Grs}	0.216	0.259	0.292	0.300	0.287	0.291	0.293	0.291
X_{Pyr}	0.121	0.141	0.107	0.123	0.128	0.127	0.009	0.013
X_{Alm}	0.484	0.513	0.522	0.517	0.508	0.523	0.446	0.527
X_{Mg}	0.200	0.215	0.170	0.192	0.201	0.195	0.020	0.024

The amounts of cations are based on 48 valencies, including 10 cations in the tetrahedral and octahedral site, to calculate the proportion of Fe^{3+}.

Table 1 (*continued*)

| Chlorite | Garnet amphibolite | | | Garnet mica-schist |
	96CH143	96CH144	96CH145	96CH156
SiO_2	26.49	26.65	24.55	23.73
TiO_2	0.03	0.01	0.07	0.02
Al_2O_3	18.78	20.18	19.15	20.99
FeO	26.56	21.32	32.22	33.23
MnO	0.74	0.15	0.39	0.66
MgO	14.33	18.22	11.29	8.94
CaO	0.04	0.03	0.04	0.02
Na_2O	0.01	0.00	0.00	0.03
K_2O	0.05	0.02	0.03	0.06
H_2O^d	11.18	11.51	10.90	10.83
Sum	98.21	98.09	98.64	98.51
Si	2.843	2.777	2.701	2.627
Al^{IV}	1.157	1.223	1.299	1.373
Al^{VI}	1.217	1.255	1.184	1.366
Ti	0.002	0.001	0.006	0.001
Fe	2.383	1.858	2.965	3.076
Mn	0.068	0.014	0.037	0.062
Mg	2.292	2.830	1.852	1.475
Ca	0.004	0.004	0.005	0.002
K	0.006	0.002	0.005	0.008
Na	0.002	0.001	0.000	0.006
OH	8.000	8.000	8.000	8.000
X_{Cchl}	0.360	0.435	0.314	0.179
X_{Daph}	0.375	0.285	0.503	0.372
X_{Mam}	0.235	0.264	0.184	0.449
X_{Mg}	0.490	0.694	0.384	0.324

The amounts of cations are based on 56 valencies.

| Epidote | 96CH143 | | 96CH144 | | 96CH145 | | 96Ch156 |
	Inclusion	Symplectite	Inclusion	Symplectite	Inclusion	Symplectite	
SiO_2	37.22	36.97	37.43	37.16	36.94	36.96	37.19
TiO_2	0.18	0.13	0.25	0.08	0.27	0.00	0.12
Al_2O_3	24.88	24.50	26.76	26.69	24.95	24.19	26.22
Fe_2O_3	11.68	12.68	8.06	9.32	11.40	12.72	8.93
MnO	0.19	0.30	0.09	0.03	0.12	0.15	0.16
CaO	23.55	23.35	23.32	23.90	23.61	23.52	22.75
H_2O^e	3.77	3.77	3.76	3.78	3.76	3.75	3.72
Sum	101.47	101.73	99.67	100.96	101.05	101.29	99.09
Si	2.959	2.943	2.982	2.944	2.948	2.955	2.964
Al^{IV}	0.041	0.057	0.018	0.056	0.052	0.045	0.036
Al^{VI}	2.290	2.242	2.496	2.436	2.294	2.234	2.493
Fe^{3+}	0.699	0.760	0.483	0.556	0.684	0.765	0.542
Ti	0.011	0.008	0.015	0.005	0.016	0.000	0.007
Mn	0.013	0.021	0.006	0.002	0.008	0.010	0.010
Ca	2.006	1.991	1.991	2.029	2.018	2.015	1.970
OH	2.000	2.000	2.000	2.000	2.000	2.000	2.000

Amounts of cations are based on 25 valencies.

Table 1 (*continued*)

Ilmenite	96CH145
TiO_2	52.27
FeO	44.04
MnO	1.89
MgO	0.09
CaO	0.13
Fe	0.939
Mn	0.041
Mg	0.003
Ca	0.004
Ti	1.002

Amounts of cations are based on six valencies.

Titanite	96CH143		96CH144		96CH145	96CH156
	inclusion		inclusion			
SiO_2	29.96	29.88	33.33	30.47	29.96	29.96
TiO_2	36.88	38.59	36.63	39.00	38.10	37.92
Al_2O_3	1.49	1.17	2.37	1.06	1.27	2.19
Fe_2O_3	0.96	0.78	0.40	0.25	0.71	0.41
MnO	0.11	0.15	0.10	0.01	0.05	0.01
CaO	28.94	28.77	27.00	28.40	28.91	28.75
H_2O^f	0.37	0.29	0.46	0.18	0.30	0.14
F	nd	nd	0.00	0.07	nd	0.61
Sum	98.71	99.63	100.29	99.67[g]	99.30	99.85[g]
Si	0.985	0.976	1.070	0.997	0.981	0.975
Ti	0.911	0.948	0.889	0.960	0.938	0.928
Al	0.058	0.045	0.090	0.041	0.049	0.084
Fe^{3+}	0.024	0.019	0.010	0.006	0.018	0.010
Ca	1.019	1.007	0.933	0.996	1.014	1.002
Mn	0.003	0.004	0.030	0.000	0.001	0.000
F	nd	nd	0.000	0.007	nd	0.055
OH	0.082	0.064	0.100	0.040	0.067	0.031
O*	4.896	4.925	4.964	4.957	4.918	4.905
$X_{Fe^{3+}}$	0.082	0.064	0.100	0.047	0.067	0.094

Sum of cations = 3; OH=(Al+Fe3+) − F. O*=[(Σ positive valencies) − OH − F]/2. nd = not determined. Cl was below detection limit.

[a] Value calculated; F, Cl, Cr, Ba are at or below detection limit numbers of generations are explained in the text.

[b] Amount calculated.

[c] Value calculated; symbols of garnet components after Kretz (1983).

[d] Value calculated; F, Cl at detection limit. Symbols: Cchl—clinochlor, Daph—daphnite and Mam—Mg-amesite.

[e] Value calculated; F, Cl at detection limit.

[f] Value calculated.

[g] Sum corrected for amount of F.

are replaced by chlorite along irregular grain boundaries. The cores contain inclusions of potassic white mica, rutile, titanite and epidote. The compositions of the dark cores correspond to tschermakitic hornblende, magnesio-hornblende or pargasitic hornblende [Si = 6.18–6.72 pfu; $(Na+K)^A$=0.37–0.87 pfu] with widely variable X_{Mg} (0.36–0.76) in different samples and generally elevated Na^B-contents (0.33–0.66 pfu). Ti contents (0.06–0.24 pfu) are also enhanced compared to Am 1, suggesting elevated temperatures of formation in line with the increased $(Na+K)^A$ and Tschermak's substitution. Scans across
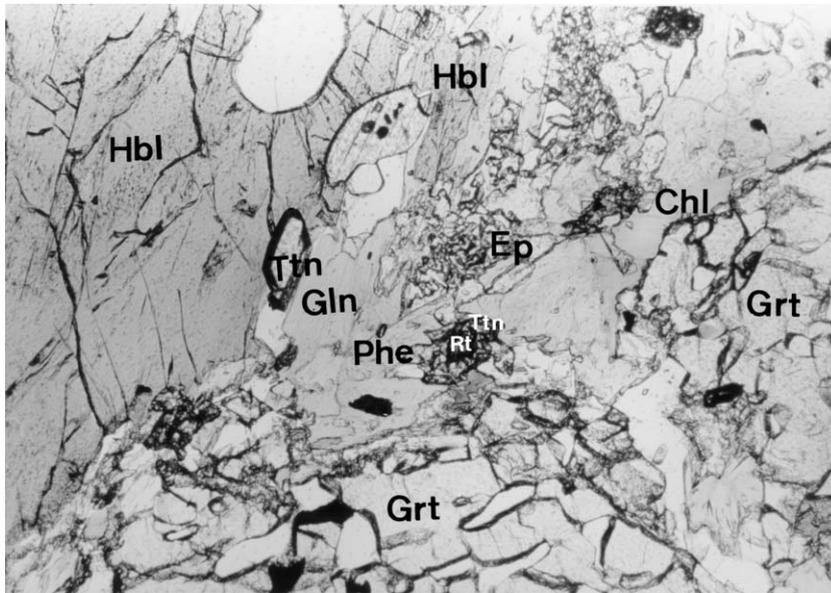
Fig. 2. The assemblage with garnet (Grt), hornblende (Hbl) and rutile (Rt) is replaced by the matrix assemblage glaucophane (Gln), phengite (Phe), chlorite (Chl), epidote symplectite (Ep) and titanite (Ttn). Sample 96CH143; plane-polarized light; width of photo is 1.6 mm.
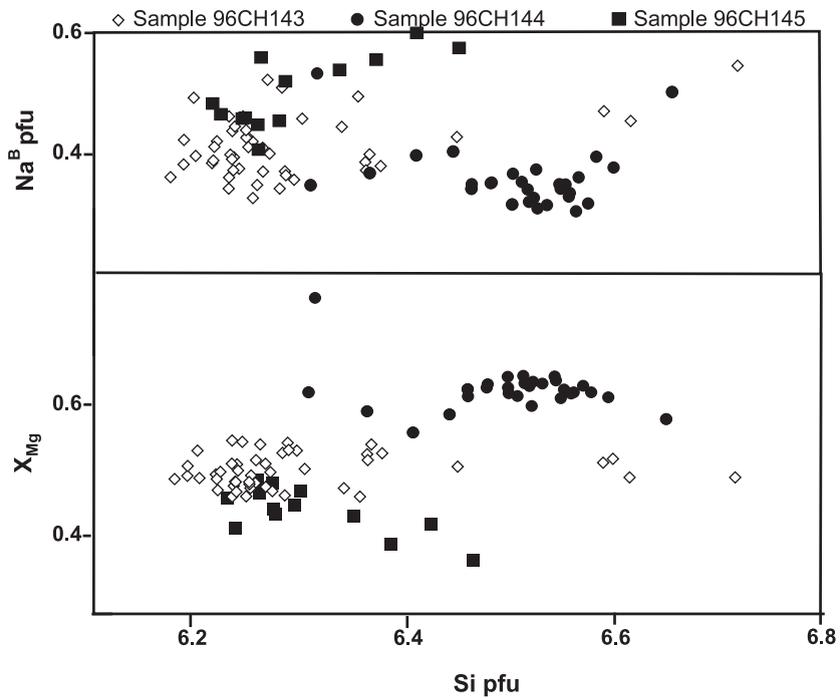

Fig. 3. Variation of X_{Mg} and Na^B with Si in hornblende (Am 2).

hornblende reveal a slight increase in Na and Al^{VI} and a decrease of Ca, Al^{IV} and X_{Mg} from core to rim. Inclusions of hornblende within or intergrown with garnet fall within this range. In all samples, the Si contents in hornblende are positively correlated with Na^B and negatively with X_{Mg} (Fig. 3). The blue amphibole rims (Am 3) are invariably glaucophane ($Na^B = 1.45 - 1.90$; $X_{Mg} = 0.48 - 0.67$; $X_{Fe^{3+}} = 0.09 - 0.35$). Scans and element distribution maps show increasing X_{Mg} and Na as well as decreasing Ca towards the outermost rim. The discontinuous boundary between both amphiboles is apparent, but zoning within both Ca- and Na-amphiboles is generally irregular and patchy. Occasional actinolite crystals (Am 4) with low Na^B (0.15 pfu) are observed at the boundary between both amphiboles.

Hypidioblastic *garnet* crystals are strongly intergrown with quartz and rich in quartz inclusions. Furthermore, green amphibole, epidote, potassic white mica, rutile and titanite were observed as inclusions or as intergrowth with the garnet rims. Alteration to chlorite at the rim and along cracks is ubiquitous. Irregular grain boundaries with replacement of garnet by both amphiboles and potassic white mica were also
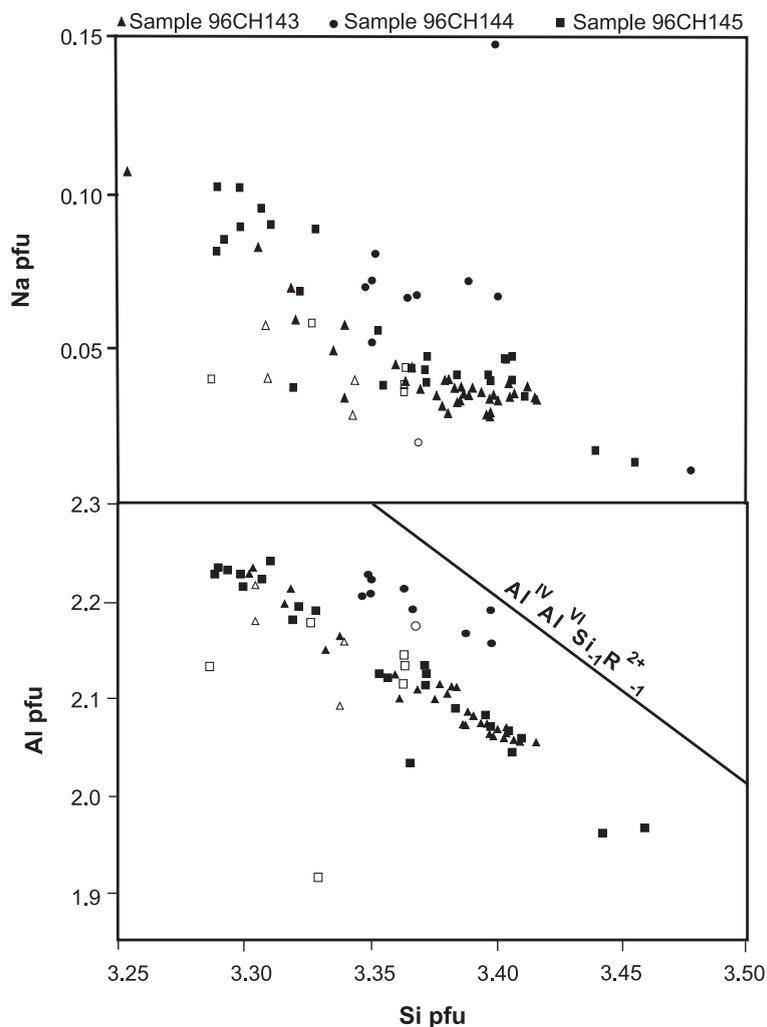
Fig. 4. Variation of Na, X_{Mg} and Al with Si of white mica. Open symbols are inclusions in garnet or hornblende, and filled symbols represent matrix white mica.

observed. Compositional variation of garnet is almandine$_{0.47-0.57}$, pyrope$_{0.11-0.20}$, grossular$_{0.20-0.34}$, spessartine$_{0.02-0.18}$ and andradite$_{0.004-0.024}$. Scans and element distribution mapping reveal a preserved prograde zoning pattern with a decrease of Mn and a slight increase of both Ca and X_{Mg} from core to rim. However, zoning is rather diffuse without sharp boundaries between the growth zones. In addition, differences between core and rim are not pronounced. Ti content in garnet shows a bimodal distribution: An enhanced TiO_2 content of 0.11–0.35 wt.% was observed near titanite inclusions and in the cores, whereas the predominant content of 0.01–0.09 wt.% occurs near the rim and near rutile inclusions.

Idioblastic *epidote* crystals are overgrown by a broad rim of epidote-quartz symplectites. The blue amphibole is intergrown with such symplectites. The Fe^{3+} content varies widely in different samples (0.45–0.79 pfu) with the highest values occurring in the symplectites, whereas epidote inclusions in garnet and hornblende generally show lower contents.

Potassic white mica is a frequent matrix phase intergrown with chlorite and hornblende, but rarely occurs as inclusion in garnet and hornblende as well. It is invariably phengite (Si = 3.25–3.47 pfu) with variable X_{Mg} (0.51–0.72) and Na (0.01–0.15 pfu), as well as some Ti (0.003–0.025 pfu), Ba (0.005–0.02 pfu) and Fe^{3+} (< 0.06 pfu). The latter is apparent in Fig. 4, where compositions plot below the line of Tschermak's substitution. In general, Na decreases with rising Si (Fig. 4). Within the white mica grains, no uniform zonation pattern exists. Inclusion white micas tend to have lower Si contents (3.28–3.34 pfu) and Na contents (0.02–0.06 pfu; Fig. 4; Table 1), but show higher calculated Fe^{3+} contents up to 0.29 pfu on the basis of 2.05 octahedral cations pfu.

Chlorite is either intergrown with matrix white mica and glaucophane or replaces garnet and hornblende. In both cases, chlorite compositions vary in a similar range (Si = 2.72–2.85 pfu; X_{Mg} = 0.38–0.63) being mainly a clinochlore daphnite solid solution with a small amesite component (10–30 mol%). Among minor elements only Mn has a notable abundance (0.01–0.10 pfu).

Albite forms patches of polygonal fabric and contains a very low anorthite component (<An$_{02}$). It was observed together with *quartz*. Ti phases are prominent minor constituents. *Rutile* occurs as inclusion in garnet and hornblende as well as in the matrix. It is often rimmed by *titanite*, which is present as large
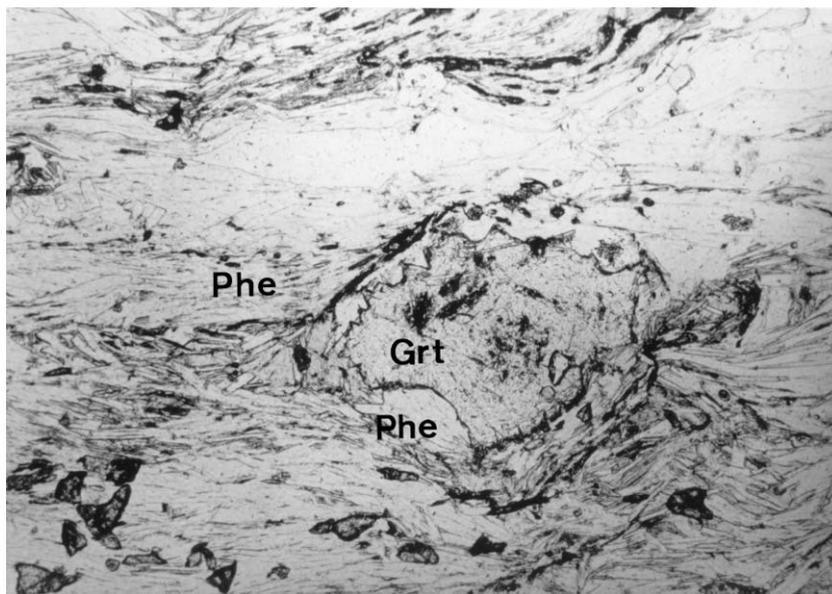

Fig. 5. Phengite (Phe) replaces garnet (Grt) grown within the s$_2$ schistosity that is defined by mimetically oriented white mica and chlorite. Sample 96CH156; plane-polarized light; width of photo is 1.6 mm.

idioblastic crystals (0.1–0.6 mm) or pods of small crystals. Titanite was also found as inclusion in garnet and hornblende showing higher Al and Fe contents and $X_{Fe^{3+}}$ than matrix titanite (Table 1). In one sample (96CH145), *ilmenite* is present as a third Ti phase. *Apatite* occurs as an accessory phase.

4.2. Garnet mica-schist

The garnet mica-schist sample (96CH-156) from the rim of an exotic block of Los Pabilos is characterized by bands of oriented white mica and chlorite with some garnet, titanite and graphite as well as accessory epidote, apatite and tourmaline. The bands are separated by polygonal quartz-albite aggregates and are overgrown by 1–3 mm sized albite porphyroblasts. The main foliation is a crenulation and transposition cleavage, as shown by recrystallised sheet silicates in hinges of microfold relics. Orientation is chiefly mimetic as evidenced by cross micas.

White mica is phengite (Si = 3.15–3.39 pfu; Na = 0.04–0.06 pfu; Ti = 0.01–0.03 pfu; Fe^{3+} < 0.1 pfu; X_{Mg} = 0.49–0.56). Chlorite (Si = 2.58–2.78 pfu) has a higher amesite component (31–49 mol%) and a less variable X_{Mg} (0.31–0.34) than in the metabasites. Among minor elements, only Mn is notable (0.04–0.07 pfu). A second type of chlorite, an olive-coloured phase with higher birefringence similar to biotite, but analytically unambiguously chlorite, displays K contents of 0.04–0.4 pfu. Backscattered electron images show that these chlorite grains are actually submicroscopically interlayered by a K-rich phase (vermiculite?). This could point to a former existence of biotite or alternatively to an alteration effect due to weathering.

Small garnet crystals (average diameter = 0.2 mm) contain tiny inclusions of quartz and rutile needles and are typically characterized by irregular concave boundaries due to replacement by (most prominently) white mica, chlorite and epidote, which often concentrically surround the garnet (Fig. 5). Compositional variation of garnet is almandine$_{0.40-0.55}$, pyrope$_{0.010-0.015}$, grossular$_{0.27-0.32}$, spessartine$_{0.14-0.32}$ and andradite$_{0.006-0.014}$ with a slight bell-shaped Mn zonation pattern and a decrease of Ca and X_{Mg} from core to rim.

Minor constituents of the garnet mica-schist are *albite* (An < 0.01), *titanite* (84–92 mol% end member component) and *epidote* (Fe^{3+} ~ 0.54 pfu).

5. Phase relationships and geothermobarometry

The most prominent feature in the garnet amphibolite is the overprint relationship of the assemblage hornblende-garnet-epidote-phengite-quartz-albite-rutile typical for the albite-epidote-amphibolite facies by the epidote blueschist facies assemblage glaucophane-phengite-chlorite-epidote-quartz-albite-titanite. First hints for an elevated pressure for the albite-epidote-amphibolite stage are unusually high contents of Na^B in hornblende and relics of omphacitic pyroxene, as reported by Kato and Godoy (1995), suggesting transition to eclogite facies conditions. The strong scatter of mineral compositions, however, suggests formation and modification of numerous local equilibria over a considerable *PT* range during the metamorphic evolution.

In order to unravel the reaction sequence in detail, to test equilibrium conditions and to quantify the conditions for stages along the *PT* path, we used two different approaches, namely (1) calculation of a net of equilibrium assemblages with varying mineral compositions from the whole rock composition and (2) calculation of *PT* conditions of local equilibria with multivariant reactions. References to the relevant thermodynamic data and calculation procedures are listed in Table 2.

5.1. PT pseudosection

The first approach involves calculation of a pseudosection in the system K_2O-Na_2O-CaO-TiO_2-Fe_2O_3-FeO-MgO-Al_2O_3-SiO_2-H_2O from the whole rock composition of sample 96CH143 (Fig. 6). The chemical analysis is given in the caption of Fig. 6. For calculating the equilibrium assemblages and respective mineral compositions, the Gibbs free energy minimization procedure was applied using the DEKAP code developed and provided by Gerya et al. (2001). This approach is based on an algorithm suggested by De Capitani and Brown (1987). The calculation of the petrogenetic grid was performed with a resolution of 5 K and 100 bar for *T* and *P*, respectively. Calculations involved the entire thermodynamic data set for minerals and aqueous fluids of Holland and Powell (1998a,b). References to applied mixing models that are consistent with this database are listed in Table 2 (method 1). Fig. 6 visualizes the stability fields of

Table 2
Thermodynamic data used for geothermobarometry

Mineral	Components	End member data	Activity formulation
Method 1			
Clinopyroxene	jadeite, diopside, hedenbergite omphacite	Holland and Powell (1998a)	Vinograd (2002a,b)
Na-amphibole	glaucophane, tremolite, tschermakite Fe-glaucophane	Holland and Powell (1998a)	Will et al. (1998)
Ca-amphibole	glaucophane, tremolite, tschermakite Fe-actinolite, pargasite	Holland and Powell (1998a)	Dale et al. (2000)
Paragonite	paragonite, margarite	Holland and Powell (1998a)	Will et al. (1998)
K-white mica	muscovite, Mg-Al-celadonite, Fe-Al-celadonite, paragonite	Holland and Powell (1998a)	Powell and Holland (1999)
Biotite	annite, phlogopite, eastonite, ordered biotite	Holland and Powell (1998a)	Powell and Holland (1999)
Chlorite	clinochlore, daphnite, Mg-amesite Al-free chlorite	Holland and Powell (1998a)	Holland and Powell (1998b)
Plagioclase	anorthite, albite	Holland and Powell (1998a)	Will et al. (1998)
Epidote	clinozoisite, epidote, Fe-epidote	Holland and Powell (1998a)	
Garnet	pyrope, almandine, grossular	Holland and Powell (1998a)	Dale et al. (2000)
Rutile, titanite, quartz magnetite, ilmenite		Holland and Powell (1998a)	$a = 1$
Method 2			
Amphibole	glaucophane	Evans (1990)	Massonne (1995a,b)
	tremolite	Berman (1988)	Massonne (1995a,b)
Chlorite	clinochlore	Massonne (1995b)	Massonne (1995a)
	daphnite	Massonne and Szpurka (1997)	as Massonne (1995a)
Epidote	clinozoisite	Berman (1988)	$a_{Clinozoisite} = 1 - X_{Pistazite}$
Garnet	grossular	Berman (1990)	Massonne (1995b)
	pyrope	Massonne (1995a,b)	Massonne (1995b)
	almandine	Berman (1990)	Massonne (1995b)
	Ti-pyrope ($Mg_3Al_2Ti_3O_{12}$)	Brandelik and Massonne (2001)	Brandelik and Massonne (2001)
K-white mica	Fe-Al-celadonite	Massonne and Szpurka (1997) Massonne (1997)	Massonne (1997)
	Mg-Al-celadonite	Massonne (1995b)	Massonne (1995b, 1997)
	muscovite	Massonne (1995b)	Massonne (1995b, 1997)
	Ti-muscovite	Massonne et al. (1993)	Massonne et al. (1993)
Plagioclase	albite	Berman (1988)	$a_{albite} = X_{albite}$
Quartz		Berman (1988)	
Method 3			
Chlorite	clinochlore	Vidal et al. (2001)	
	daphnite	Vidal et al. (2001)	
	Mg-amesite	Vidal et al. (2001)	
K-white mica	muscovite	Parra et al. (2002a,b)	
	Mg-Al-celadonite	Parra et al. (2002a,b)	
	Fe-Al-celadonite	Parra et al. (2002a,b)	

high-variance mineral assemblages at defined *PT* conditions for the selected garnet amphibolite composition. The aim of this approach is to unravel an overall trend of the *PT* path and particularly to yield information on the relative position of the prograde *PT* path that cannot be obtained otherwise.

In six stability fields that will be shown to be passed by the proposed *PT* path, we selected representative points A–F and extracted calculated mineral assemblages and compositions (Table 3) for comparison with the measured compositions of minerals grown during successive stages of equilibration
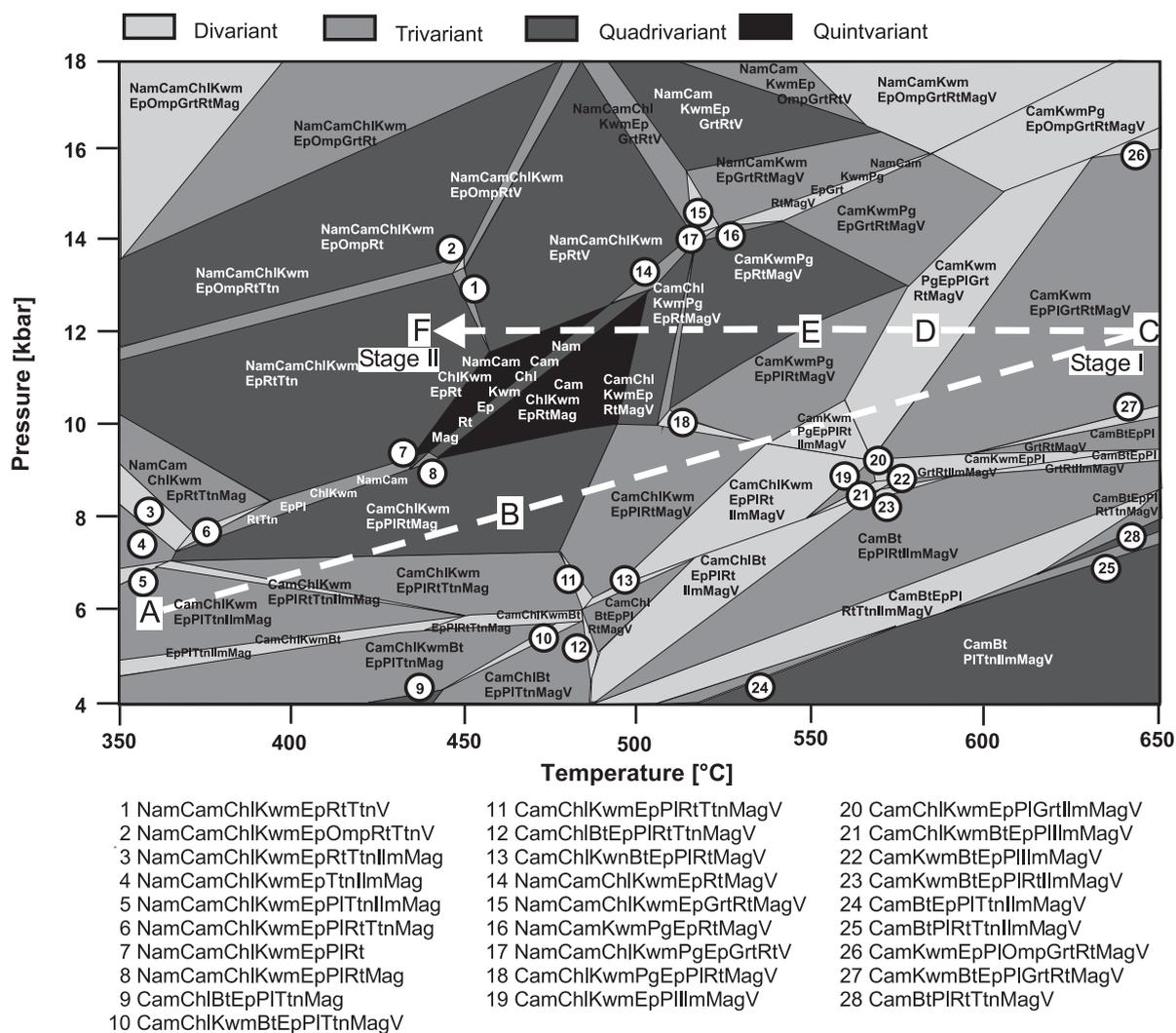
Fig. 6. $P-T$ pseudosection for garnet amphibolite sample 96CH143 calculated with the following components (wt.% in whole rock given in brackets): SiO_2 (47.87)-TiO_2 (1.93)-Al_2O_3 (14.27)-Fe_2O_3 (3.49)-FeO (9.93)-MgO (5.50)-CaO (9.90)-Na_2O (2.66)-K_2O (0.73)-H_2O (2.59). All calculated assemblages contain additional quartz. For thermodynamic data and activity models, see Table 2. A possible PT path discussed in the text is given by the sequence of points A to F (for mineral compositions, see Table 3). Abbreviations not included in Kretz (1983) are: Kwm—K-white mica; Nam—Na-amphibole; Cam—Ca-amphibole; V—vapour. Analyses were done at Ruhr-Universität Bochum by XRF except Fe^{2+} and H_2O (standard wet chemical methods).

(Table 1). The relative changes in calculated mineral assemblages provide a possible reaction sequence that can be compared with the petrological data. However, this approach is not only dependent on the thermodynamic data set and the activity models used, but also on the assumption that the whole rock was the reaction space for equilibrium conditions at any transitional stage of the PT path. In addition, Mn

was disregarded and Fe^{3+} not assigned to garnet, micas and amphiboles. As a result, there are systematic differences between calculated and recorded mineral compositions. Nevertheless, the predicted reaction sequence corresponding to changes in mineral assemblages along the $P-T$ path is proved by observed mineral relationships and some compositional trends along the inferred $P-T$ path in the

Table 3
Calculated mineral compositions at defined points in pseudosection of Fig. 6

(A) 6 kbar/360 °C, CamKwmChlEpPlTtnIlmMagQtz		(B) 8 kbar/460 °C, CamKwmChlEpPlRtMagQtz	
Cam	$Na_{0.16}(Ca_{1.62}Na_{0.38})(Fe_{1.86}Mg_{2.76}Al_{0.38})(Al_{0.16}Si_{7.84})O_{22}(OH)_2$	Cam	$Na_{0.24}(Ca_{1.55}Na_{0.45})(Fe_{2.07}Mg_{2.48}Al_{0.45})(Al_{0.22}Si_{7.78})O_{22}(OH)_2$
Kwm	$(K_{0.95}Na_{0.05})(Fe_{0.39}Mg_{0.05}Al_{1.56})(Al_{0.56}Si_{3.44})O_{10}(OH)_2$	Kwm	$(K_{0.92}Na_{0.08})(Fe_{0.39}Mg_{0.06}Al_{1.55})(Al_{0.55}Si_{3.45})O_{10}(OH)_2$
Chl	$(Fe_{2.84}Mg_{2.15}Al_{1.01})(Al_{1.00}Si_{3.00})O_{10}(OH)_8$	Chl	$(Fe_{2.84}Mg_{2.14}Al_{1.02})(Al_{1.01}Si_{2.99})O_{10}(OH)_2$
Ep	$Ca_2Al_2(Al_{0.38}Fe_{0.62})Si_3(OH)$	Ep	$Ca_2Al_2(Al_{0.29}Fe_{0.71})Si_3(OH)$
Pl	$(Na_{0.95}Ca_{0.05})(Al_{1.05}Si_{2.95})O_8$	Pl	$(Na_{0.94}Ca_{0.06})(Al_{1.06}Si_{2.94})O_8$
(C) 12 kbar/650 °C, CamKwmEpPlGrtRtMagQtz		(D) 12 kbar/580 °C, CamKwmPgEpPlGrtRtMagQtzV	
Cam	$Na_{0.29}(Ca_{1.55}Na_{0.45})(Fe_{1.77}Mg_{2.70}Al_{0.53})(Al_{0.38}Si_{7.62})O_{22}(OH)_2$	Cam	$Na_{0.34}(Ca_{1.41}Na_{0.59})(Fe_{1.97}Mg_{2.44}Al_{0.59})(Al_{0.31}Si_{7.69})O_{22}(OH)_2$
Kwm	$(K_{0.94}Na_{0.06})(Fe_{0.25}Mg_{0.09}Al_{1.66})(Al_{0.66}Si_{3.34})O_{10}(OH)_2$	Kwm	$(K_{0.88}Na_{0.12})(Fe_{0.30}Mg_{0.07}Al_{1.63})(Al_{0.63}Si_{3.37})O_{10}(OH)_2$
Grt	$(Fe_{1.92}Mg_{0.28}Ca_{0.80})Al_2Si_3O_{12}$	Pg	$(Na_{0.97}Ca_{0.03})(Al_{3.03}Si_{2.97})O_{10}(OH)_2$
Ep	$Ca_2Al_2(Al_{0.30}Fe_{0.70})Si_3(OH)$	Grt	$(Fe_{2.07}Mg_{0.19}Ca_{0.74})Al_2Si_3O_{12}$
Pl	$(Na_{0.83}Ca_{0.17})(Al_{1.17}Si_{2.83})O_8$	Ep	$Ca_2Al_2(Al_{0.34}Fe_{0.66})Si_3(OH)$
		Pl	$(Na_{0.91}Ca_{0.09})(Al_{1.09}Si_{2.91})O_8$
(E) 12 kbar/550 °C, CamKwmPlPgEpRtMagQtzV			
Cam	$Na_{0.31}(Ca_{1.39}Na_{0.61})(Fe_{2.11}Mg_{2.27}Al_{0.62})(Al_{0.31}Si_{7.69})O_{22}(OH)_2$	(F) 12 kbar/440 °C, NamCamKwmChlEpRtTtnQtz	
Kwm	$(K_{0.86}Na_{0.14})(Fe_{0.36}Mg_{0.07}Al_{1.57})(Al_{0.58}Si_{3.42})O_{10}(OH)_2$	Nam	$(Na_{1.83}Ca_{0.17})(Fe_{1.42}Mg_{1.75}Al_{1.83})Si_{8.00}O_{22}(OH)_2$
Pg	$(Na_{0.98}Ca_{0.02})(Al_{3.02}Si_{2.98})O_{10}(OH)_2$	Cam	$Na_{0.18}(Ca_{1.46}Na_{0.54})(Fe_{2.13}Mg_{2.33}Al_{0.52})(Al_{0.20}Si_{7.80})O_{22}(OH)_2$
Ep	$Ca_2Al_2(Al_{0.30}Fe_{0.70})Si_3(OH)$	Kwm	$(K_{0.93}Na_{0.07})(Fe_{0.52}Mg_{0.07}Al_{1.41})(Al_{0.41}Si_{3.59})O_{10}(OH)_2$
Pl	$(Na_{0.94}Ca_{0.06})(Al_{1.06}Si_{2.94})O_8$	Chl	$(Fe_{3.15}Mg_{1.84}Al_{1.01})(Al_{1.01}Si_{2.99})O_{10}(OH)_8$
		Ep	$Ca_2Al_2(Al_{0.32}Fe_{0.68})Si_3(OH)$

pseudosection are comparable with observed compositional trends.

Recorded transitional prograde compositions are only given by some Ca-amphibole inclusions (Am 1a, Am 1b) in garnet and hornblende. These amphibole inclusions contain elevated Na^B similar to the calculated amphibole compositions at A and B that points to already elevated metamorphic pressure. The sequence of recorded amphibole compositions Am 1a–Am 1b–Am 2 show increasing Na^A and Al^{IV} due to prograde temperature increase as the sequence of calculated compositions A–B–C does. This prograde sequence toward the stability field of garnet (>550 °C) must have occurred above the stability field of biotite that does not occur as a relic phase (upper limit at 350 °C/5 kbar to 550 °C/8 kbar) and below the appearance of Na-amphibole (lower limit 350 °C/7 kbar to 550 °C/14 kbar). The Ca-amphibole relics presumably coexisted partly with prograde titanite that also occurs as inclusion in garnet. Compositions of amphiboles Am 1a and Am 1b of sample 96CH143 are roughly comparable with calculated compositions at points A (with coexisting titanite) and B (after titanite breakdown) defining two possible, but non-unique prograde stages of the *PT* path. Calculated Fe contents of epidote and elevated Si contents of white mica at points A and B are in line with those recorded

as inclusions in garnet. According to the above hints, the prograde *PT* path most likely passed through the high-pressure part of the greenschist facies roughly parallel to a geothermal gradient of ∼ 15 °C/km.

Conditions for the peak of metamorphism (stage I) are defined by stability fields covering assemblages with garnet-hornblende at $T > 560$ °C and $P = 9.5–16$ kbar bounded towards lower and higher pressures by assemblages with biotite and omphacite, respectively (Fig. 6). Chlorite, titanite and ilmenite were not stable at these conditions. Similar to representative calculated mineral compositions (C and D in Table 3; Fig. 6) also the measured composition of the peak metamorphic hornblende (Am 2; Table 1) shows highest Na^A, Na^B, Al^{IV} and X_{Mg} in the prograde reaction sequence. However, the Na^A and Si contents are too low and too high, respectively, when compared with the measured compositions. This can be observed at most conditions of the pseudosection. This inconsistency might also be due to metasomatic changes of the whole rock composition during the retrograde *PT* path (see below; Section 6). Calculated plagioclase compositions show an increasing anorthite component, up to oligoclase composition at C. However, the recorded plagioclase composition is pure albite only. Epidote composition varies little in line with the analysed compositions. Towards point E with decreasing tem-

perature at constant elevated pressure, garnet becomes unstable: Calculated hornblende compositions C−E show slight increase of Si and Na^B and a decrease in X_{Mg}. This is reflected by a similar trend observed in the zonation pattern of the hornblende from core to rim (see Section 4.1) and the variation of its recorded compositions (Fig. 3). It must be noted that these trends contrast a possible prograde path. Appearance of paragonite on the early retrograde path at points D and E cannot be corroborated for the studied samples. This is in line with evidence provided in the following Section 5.2 that no peak metamorphic white mica compositions are preserved at all.

The retrograde epidote-blueschist facies stage II caused breakdown of garnet and hornblende with concomitant growth of glaucophane and chlorite as new phases not stable at $T > 500$ °C as well as growth of titanite around rutile. Stage II is confined to a stability field of assemblages with Na-amphibole, but without omphacite, at 350–460 °C and 7–12 kbar. Assemblages with lawsonite occurred at pressures >18 kbar at 300 °C outside the chosen PT field for the pseudosection. The calculated composition of the Na-amphibole at F (Table 3; Fig. 6) is compatible with the analyzed one (Am 3). The same is valid for the calculated composition of the coexisting Ca-amphibole and the rarely observed retrograde actinolite (Am 4). Hence, both amphiboles might have coexisted at this stage. Alternatively, it might represent a later retrograde stage. The calculated Si content of the white mica at F is the highest within the reaction sequence C−F, in line with the highest values recorded in matrix micas. In the same isobaric sequence, C−F Na decreases with increasing Si. This is in line with the recorded trend in Fig. 4. It must be noted that the negative Na−Si correlation would contrast a prograde trend of rising P and T. Inclusion white micas have lower Si and Na contents. Calculated and recorded chlorite compositions for stage II are also compatible.

The pseudosection approach also allows to assess amounts of free hydrous fluids that must be available to produce the retrograde assemblage during isobaric cooling at high pressures. In the calculated sequence of assemblages C−F, a continuous systematic decrease of the ratio free H_2O/total H_2O from 0.47 to 0.00 can be observed. The consumption of ∼ 1.22 wt.% of free H_2O (with 2.59 wt.% H_2O in the system) provides a minimum amount of water added during cooling assuming that only the analysed water content of the rock was available in the system and that reactions were instantaneous and complete. If excess H_2O is available, a maximum amount of 2.49 wt.% can be consumed for the complete growth of the blueschist assemblage. Under the common assumption that free water leaves the system at peak metamorphic conditions, a considerable amount of water must have been added again by external fluid infiltration on the retrograde path.

Summarizing the overall compositional evolution of the amphiboles along the PT path can qualitatively be compared in Fig. 7 for calculated and recorded contents of Al^{IV} and Al^{VI}. As Al^{IV} is particularly temperature-sensitive and Al^{VI} rather pressure-sensitive (e.g. Triboulet, 1992), the recorded trend resembles the overall counterclockwise trend of the PT path. It must be noted that above interpretation of the pseudosection is a semiquantitative approach mainly constraining the tendency of the PT trajectory by comparing relative compositional trends. This still leaves room for the exact position of the PT path.

5.2. Multivariant equilibria

In addition to the PT pseudosection, we calculated multivariant reactions with the actual compositions of minerals in close contact, because the whole rock can certainly not be regarded as a closed reaction space particularly after peak metamorphic conditions were reached. This second approach can also be used as a test, whether local equilibrium was attained or not. Recently, Vidal and Parra (2000) and Parra et al. (2002a,b) were able to show that a series of local equilibria on thin section scale may exist in HP−LT metapelites which constrain particularly the shape of the early retrograde PT path during recrystallisation and crystallisation of new grains.

Multivariant equilibria calculations were undertaken mainly using the Ge0-Calc software of Brown et al. (1989) and derivations (TWQ) with the thermodynamic data set of Berman (1988) with different additions and activity models as summarized in Table 3 (methods 2 and 3). Results are plotted into Fig. 8 which contains a reference frame of multivariant boundary reactions around the albite-epidote-amphibolite facies as proposed by Evans (1990) including formation of garnet
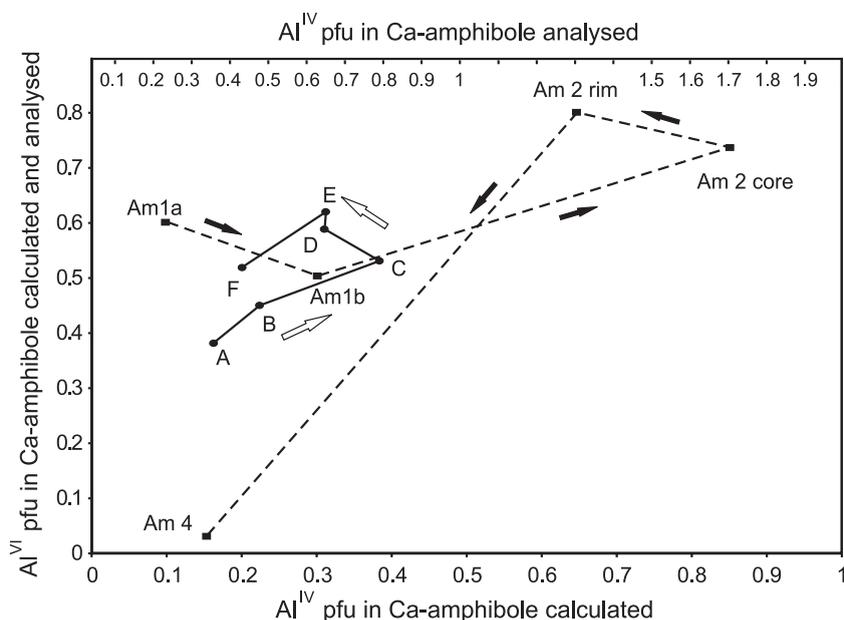
Fig. 7. Comparison of the compositional evolution of the calculated (method 1) Ca-amphibole generations (A–F; see Fig. 6; Table 3) and the recorded Ca-amphibole generations (Am 1–4; Table 1) for Al^{IV} versus Al^{VI} in sample 96CH143.

represented by its pyrope component. These were calculated (method 2) for mean idealized compositions observed in the studied rocks and a hypothetical intermediate plagioclase composition typically observed in low pressure amphibolites. Because compositions do not vary along these boundaries as in the pseudosection approach due to the applied method, this frame is set only for the purpose of visualization.
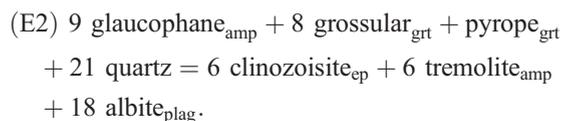
5.2.1. Stage I

With the relics of the prograde PT path, we are not able to calculate transient prograde PT conditions due to the lack of coexisting phases. By attempting equilibria calculation for the peak metamorphic conditions (stage I) involving hornblende and garnet, we found that reactions with white mica resulted in unrealistically high P and T values, for instance, according to the equilibrium:

(E1) almandine$_{grt}$ + 3 Mg-Al-celadonite$_{wm}$

   = 3 Fe-Al-celadonite$_{wm}$ + pyrope$_{grt}$.
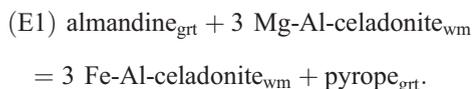
This suggests disequilibria, i.e. that the white mica in contact or included in garnet represents lower

temperature compositions attained at lower temperatures either of the prograde PT path or of the retrograde path with modified Fe/Mg ratios. The same observation can also be made for the garnet mica-schist. This is in line with the finding that white mica replaces garnet at its rims. Furthermore, it was shown in Section 5.1 that chlorite was not a stable phase with garnet. This considerably reduces the number of phases that can be used for PT estimates of stage I. Therefore, we calculated the following water-independent barometer equilibrium E2 (using method 2, Table 3) for 17 local coexisting pairs of garnet and hornblende (inclusions or intergrowth near the garnet rims):

(E2) 9 glaucophane$_{amp}$ + 8 grossular$_{grt}$ + pyrope$_{grt}$

   + 21 quartz = 6 clinozoisite$_{ep}$ + 6 tremolite$_{amp}$

   + 18 albite$_{plag}$.

Although it is unsecured, if nearly pure albite existed at peak metamorphic conditions (see Section 5.1), a slight reduction of its activity has minor influence on the position of this equilibrium. The spectrum of variation is plotted as line 7 in Fig. 8.
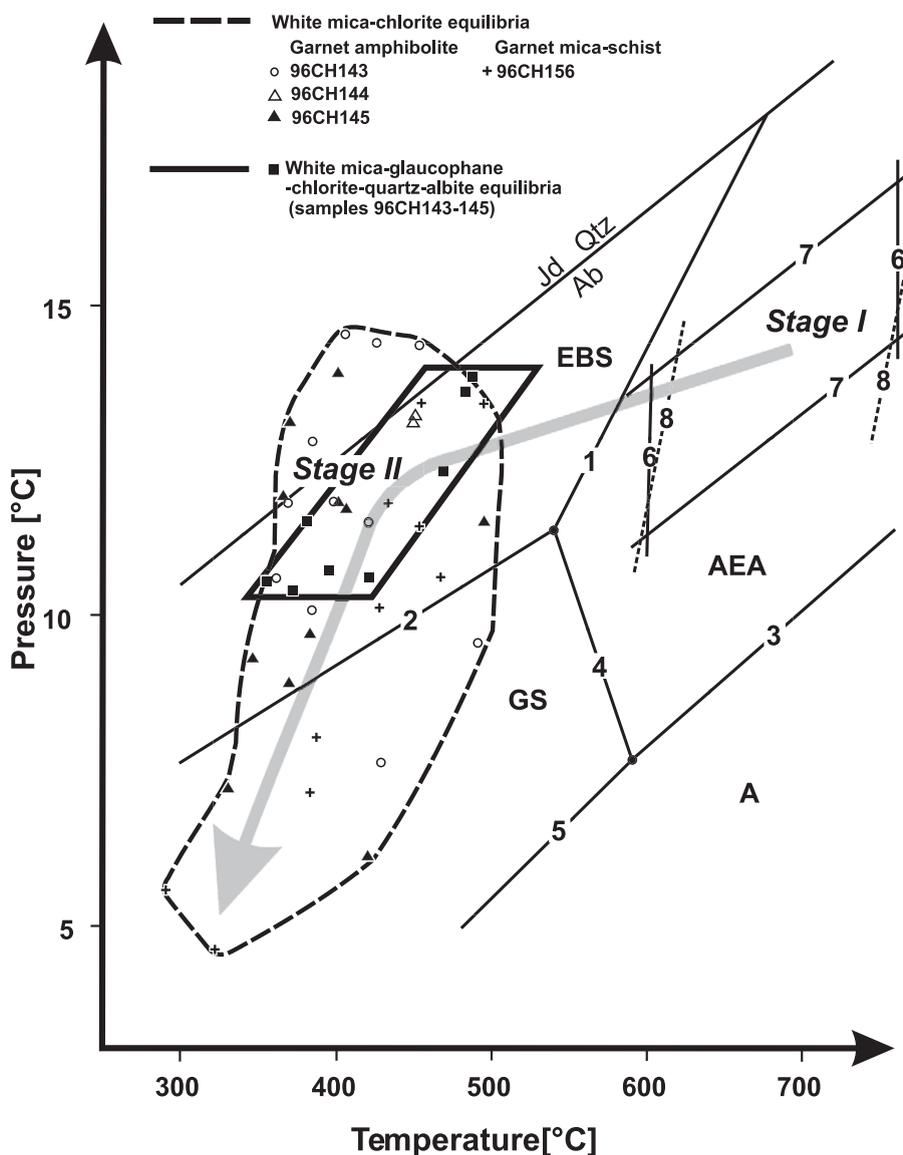
Fig. 8. *PT* path derived by calculating multivariant reactions. Facies fields: GS = greenschist; EBS = epidote blueschist; AEA = albite-epidote-amphibolite; A = amphibolite. Multivariant facies boundary reactions (1) Ab + Chl + Tr = Gln + Czo + Qtz + V, (2) Chl + Czo + Qtz = Prp + Tr + V, (3) Chl + Czo + Qtz = An + Tr + V, (4) Prp + Czo + H2O = An + Tr + V, (5) Gln + Czo + Qtz = Ab + Prp + Tr + V are calculated with intermediate idealized compositions for the garnet amphibolite: Na-amphibole (a_{Gln} = 0.645; a_{Tr} = 0.430); Ca-amphibole (a_{Gln} = 0.284; a_{Tr} = 0.719); chlorite (a_{Chl} = 0.099); garnet (a_{Prp} = 0.005); epidote (a_{Czo} = 0.3); plagioclase (a_{An} = 0.4). The albite breakdown reaction is taken from Holland (1980). Stage I: (6) temperature limits for Fe–Mg exchange between hornblende and garnet. (7) Range of reaction Gln + Grs + Prp + Qtz = Czo + Tr + Ab for coexisting Grt-Hbl-Ep-Qtz-Ab. (8) Temperature limits by the Ti-in-garnet thermometer. For stage II, see box for signatures and methods used. For further explanation, see text.

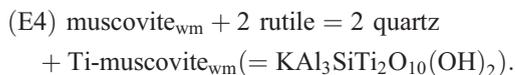For the same garnet-hornblende pairs, temperatures were calculated using conventional garnet-amphibole Fe–Mg exchange thermometry (Graham and Powell, 1984; line 6 in Fig. 8). The resulting high-temperature range is also corroborated by the high-Ti contents in hornblende which are typical for amphiboles of the

upper amphibolite facies (Raase, 1974). Coinciding temperature results were also obtained by calculation of the equilibrium

(E3) $\text{pyrope}_{grt} + 3 \text{ rutile} = 3 \text{ quartz} + \text{Ti} - \text{pyrope}_{grt}$

$$(= Mg_3Al_2Ti_3O_{12})$$
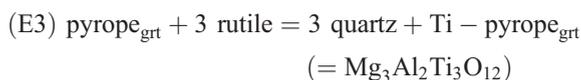
calibrated by Brandelik and Massonne (2001). For the low-Ti contents in garnet near rutile inclusions, the calculated temperature range is indicated by line 8 in Fig. 8. Summarizing for stage I, a wide *PT* range of 600–764 °C, 11.0–16.5 kbar results. This range is consistent with the prediction from the pseudosection (Fig. 6).

It remains surprising that white mica compositions are not preserved for these conditions. Otherwise, a potential independent proof of maximum pressures reached could be obtained by the Ti-in-phengite geobarometer (Massonne et al., 1993) which is related to the equilibrium

(E4) $\text{muscovite}_{wm} + 2 \text{ rutile} = 2 \text{ quartz}$

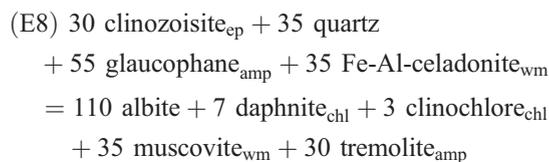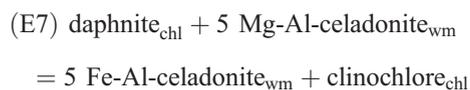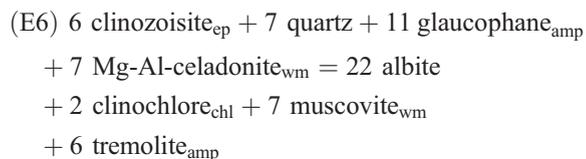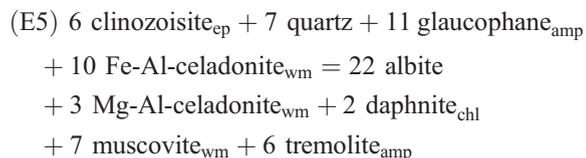$+ \text{Ti-muscovite}_{wm}(= KAl_3SiTi_2O_{10}(OH)_2).$

Rutile + quartz were present during a considerable part of the *PT* path. However, calculating white micas with the highest Ti contents resulted in pressures of 19.8 (550 °C)–22.3 (640 °C), when coexistence with rutile is assumed. However, such conditions would mean that during the prograde *PT* path and around peak *PT* conditions albite should have broken down to omphacite in all studied samples, and barroisitic amphibole typical for HT eclogites should be present. This negative result is a further evidence that no peak metamorphic white mica compositions coexisting with rutile have been detected in our garnet amphibolite samples.
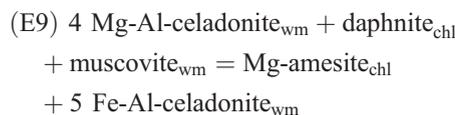
5.2.2. Stage II

To determine conditions of glaucophane formation (stage II), equilibria involving coexisting chlorite-glaucophane-phengite-albite-quartz were calculated using a set of data which also accounts for estimated Fe^{2+}/Fe^{3+} ratios in amphibole and white mica (method 2; Table 3). This method was successfully tested by Willner et al. (2000, 2001) for metabasites of the Chilean Coastal Cordillera. The following set
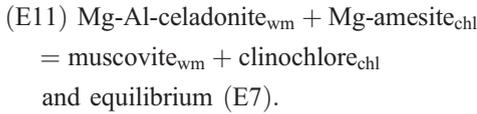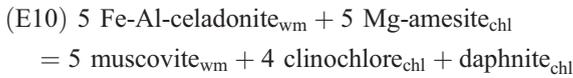
of water-independent multivariant equilibria were calculated:

(E5) $6 \text{ clinozoisite}_{ep} + 7 \text{ quartz} + 11 \text{ glaucophane}_{amp}$

$+ 10 \text{ Fe-Al-celadonite}_{wm} = 22 \text{ albite}$

$+ 3 \text{ Mg-Al-celadonite}_{wm} + 2 \text{ daphnite}_{chl}$

$+ 7 \text{ muscovite}_{wm} + 6 \text{ tremolite}_{amp}$

(E6) $6 \text{ clinozoisite}_{ep} + 7 \text{ quartz} + 11 \text{ glaucophane}_{amp}$

$+ 7 \text{ Mg-Al-celadonite}_{wm} = 22 \text{ albite}$

$+ 2 \text{ clinochlore}_{chl} + 7 \text{ muscovite}_{wm}$

$+ 6 \text{ tremolite}_{amp}$

(E7) $\text{daphnite}_{chl} + 5 \text{ Mg-Al-celadonite}_{wm}$

$= 5 \text{ Fe-Al-celadonite}_{wm} + \text{clinochlore}_{chl}$

(E8) $30 \text{ clinozoisite}_{ep} + 35 \text{ quartz}$

$+ 55 \text{ glaucophane}_{amp} + 35 \text{ Fe-Al-celadonite}_{wm}$

$= 110 \text{ albite} + 7 \text{ daphnite}_{chl} + 3 \text{ clinochlore}_{chl}$

$+ 35 \text{ muscovite}_{wm} + 30 \text{ tremolite}_{amp}$

Calculated *P–T* data from (E5) to (E8), covering the entire compositional spectrum of phases coexisting at stage II, lie in the range 10–14 kbar, 350–500 °C (see box in Fig. 8) reflecting the conditions of glaucophane formation. However, during further decompression into the greenschist field no amphibole was newly formed as it can be observed in virtually all metabasites of the Western Series (Willner et al., 2000, 2001). This is probably due to decreasing availability of a fluid phase at the latest stage of metamorphism.

For coexisting chlorite and white mica in the matrix of the garnet amphibolite and the garnet mica-schist samples, we calculated the following set of water-independent multivariant equilibria using the reference data of an independent method developed and tested by Vidal and Parra (2000) and Parra et al. (2002a,b) especially for metapelites in similar HP–LT terranes (method 3; Table 2):

(E9) $4 \text{ Mg-Al-celadonite}_{wm} + \text{daphnite}_{chl}$

$+ \text{muscovite}_{wm} = \text{Mg-amesite}_{chl}$

$+ 5 \text{ Fe-Al-celadonite}_{wm}$

(E10) 5 Fe-Al-celadonite$_{wm}$ + 5 Mg-amesite$_{chl}$

  = 5 muscovite$_{wm}$ + 4 clinochlore$_{chl}$ + daphnite$_{chl}$

(E11) Mg-Al-celadonite$_{wm}$ + Mg-amesite$_{chl}$

  = muscovite$_{wm}$ + clinochlore$_{chl}$

  and equilibrium (E7).

All analysed iron was assumed to be ferrous in this approach. Other possible end members with contents in chlorite and mica of less than 5% (e.g. sudoite, pyrophyllite) could not be considered because of the high uncertainty of their activity in these phases. Method 3 yielded a systematic scatter of PT data in the range 300–500 °C and 4.5–14.5 kbar and a slope following the retrograde PT path (Fig. 8) as observed in other blueschist terranes (Vidal and Parra, 2000). The PT data and their scatter for the three metabasite samples analysed and the adjacent garnet mica-schist (sample 96CH156) are identical suggesting that both rock types had at least a common retrograde history. There is a good coincidence of the upper part of this range of equilibria with a similar slope of decreasing P and T for the formation of glaucophane derived by method 2. However, only white mica and chlorite appear to have equilibrated further down to ~ 5 kbar and 300 °C, i.e. outside the stability of the blueschist assemblage.

As crystallisation of minerals was strain-free during the entire PT path within the metabasites, results show that local fluid access during the retrograde PT path controlled the chemical variations of recrystallised or newly formed chlorite and white mica at thin section scale. Equilibrium is achieved only locally and during given PT conditions there is little reequilibration of coexisting white mica and chlorite. It is likely that either the fluid was continuously buffered by the given mineral assemblage, or that during prolonged periods the rock was devoid of hydrous fluids. However, a long-term fluid influx during stage II and during the retrograde path evidently led to an entire recrystallisation and neocrystallisation of matrix white mica such that it was no longer in equilibrium with garnet of stage I.

Comparing the results of the principal geothermobarometric approaches (methods 1–3) near isobaric cooling by about 300 °C at around 12–14 kbar is likely for the early retrograde metamorphic evolution.

The calculation of multivariant equilibria also shows that the dominant matrix phases white mica and chlorite partially re-equilibrated during decompression down to 5 kbar and 300 °C. It is notable that the retrograde decompression path of the garnet mica-schist is identical to that of the garnet amphibolite. The pseudosection approach shows that the prograde PT path passed through the high-pressure part of the greenschist facies field. Hence, for the garnet amphibolite a complete counterclockwise PT trajectory can be derived.

6. Geochronological results

We analysed the Rb–Sr isotopic system for different matrix minerals and mineral size fractions from the garnet amphibolite 96CH161 (Fig. 9a; Table 4) and the garnet mica-schist 96CH156 (Fig. 9b; Table 4). For the garnet amphibolite, apatite, titanite and epidote as well as two white mica grain size fractions (i.e. the blueschist facies, stage II equilibrium assemblage) define an isochrone with an age of 305.3 ± 3.2 Ma (n = 5, MSWD = 0.46). For the garnet mica-schist, apatite, quartz + feldspar, and three white mica grain size fractions yield an age of 296.6 ± 4.7 Ma (n = 5, MSWD = 59). Both isochron ages can be interpreted as crystallisation ages for the respective metamorphic assemblages. They do not reflect cooling ages. This is because temperature-controlled isotopic closure during (slow) cooling would produce two critical phenomena, which are both not observed in our data set (see also Glodny et al., 2002b, 2003). First, the classical theory of isotopic closure predicts higher apparent ages for larger white mica grains and younger ages for small grains, i.e. a grain size dependence of apparent ages. In both samples, the white mica grains were split into different sieve fractions, which all show identical apparent ages within limits of error. Second, if at or above the white mica closure temperature Sr would have been mobile in the rock, it would have been incorporated in an irregular way into the other phases. This process would have led to destruction of the isochron correlation, at least in sample 96CH161. Here, however, the isochron correlation is perfect. The 304 ± 9-Ma K–Ar age of white mica in the Los Pabilos amphibolite mentioned by Kato and Godoy (1995),
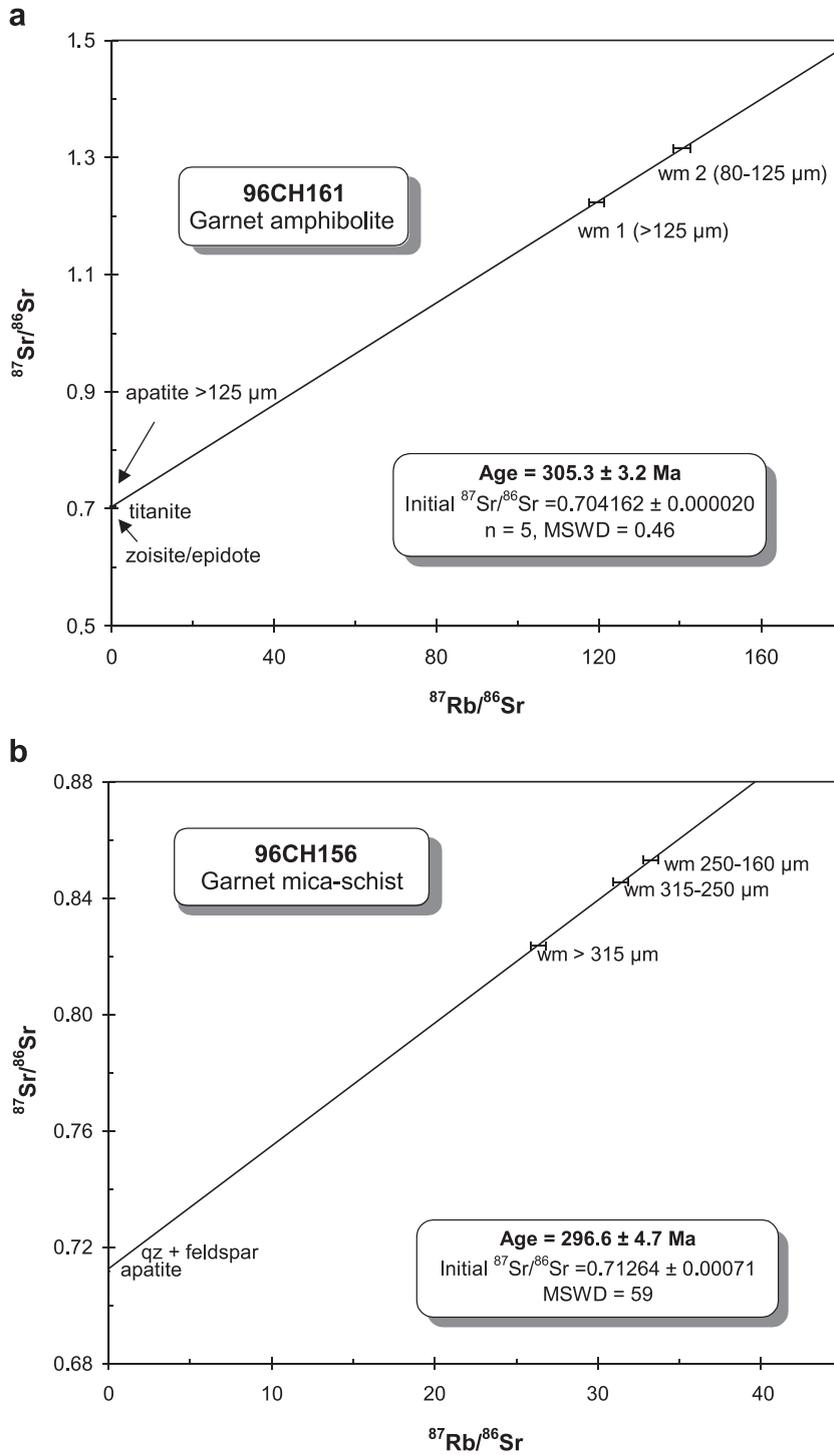
a

b

Fig. 9. (a) Rb–Sr mineral isochron for garnet amphibolite sample 96CH161. (b) Rb–Sr mineral isochron for garnet mica-schist sample 96CH156.

Table 4
Rb/Sr analytical data

Sample no., analysis no.	Material	Rb [ppm]	Sr [ppm]	$^{87}Rb/^{86}Sr$	$^{87}Sr/^{86}Sr$	$^{87}Sr/^{86}Sr$, $2\sigma_m$ [%]
96CH161 (305.3 ± 3.2 Ma (excl. hbl), MSWD = 0.46, Sr_i = 0.704162 ± 0.000020; incl. hbl: 304.4 ± 4.3 Ma, MSWD = 2.4)						
PS739	wm 1>125 μm	247	6.30	119.4	1.222454	0.0016
PS746	wm 2 80–125 μm	262	5.73	140.4	1.315169	0.0034
PS745	zoisite/epidote	0.14	766	0.0006	0.704181	0.0014
PS721	apatite>125 μm	0.08	327	0.0007	0.704157	0.0016
PS757	titanite	0.34	25.2	0.0397	0.704326	0.0014
PS810	hornblende	5.31	21.5	0.713	0.707161	0.0014
96CH156 (296.6 ± 4.7 Ma, MSWD = 59, Sr_i = 0.71264 ± 0.00071)						
PS855	apatite	3.66	705	0.0150	0.712352	0.0012
PS856	wm 315–250 μm	455	41.8	31.91	0.846991	0.0018
PS857	wm>315 μm	443	49.0	26.43	0.824062	0.0014
PS858	wm 250–160 μm	452	40.3	32.89	0.851797	0.0016
PS873	quartz + feldspar	8.49	19.2	1.281	0.718427	0.0012

Errors are reported at the 2σ level. An uncertainty of ± 1% has to be assigned to Rb/Sr ratios. wm: white mica; hbl: hornblende.

virtually identical to our result for the same rock, similarly indicates that the age value of ~ 305 Ma is (or is very close to) an assemblage crystallisation age. Otherwise, it would be difficult to explain the coincidence of Rb–Sr mineral and K/Ar white mica ages since the K–Ar system is classically believed (see Villa, 1998) to have a much lower closure temperature than the Rb–Sr system.

The well-defined isochrons date the retrograde equilibration during stage II and the early decompression stage, during which influx of external fluids occurred. Nevertheless, stage I minerals may be significantly older than the stage II assemblages, but we were not able to date the stage I equilibration with our methods. For stage I minerals, we only obtained isotope data for hornblende of sample 96CH161. These show that hornblende indeed slightly differs isotopically from stage II minerals. Its Rb–Sr system plots slightly *below* the stage II isochron, indicating that there was no complete isotopic rehomogenization of Sr during the retrograde stage at high-temperature cooling stages. Rather metasomatism during the blueschist stage must have been effective. The penetrating external fluids at this stage probably had higher $^{87}Sr/^{86}Sr$ ratios than the original metabasic whole rock. This is reasonable bearing in mind that most fluids must have been generated by dehydration of the dominating continent-derived metapsammopelites of the accretionary system. As a result, the stage II assemblage equilibrated at a higher initial $^{87}Sr/^{86}Sr$ ratio than that present in hornblende of stage I at the same time. The metasomatic effect would be an independent proof of external fluid influx during stage II.

In view of our finding that both the garnet amphibolite and the garnet mica-schist equilibrated within exactly the same retrograde *PT* range, the evident difference of the resulting ages of 8.7 Ma would mean that the two rocks passed through this stage at slightly different times. This is easily explained when considering that continuous subduction mass flow circulation will lead to continuous tectonic reorganization of the accretionary complex and therefore to possible tectonic juxtaposition of rocks which passed through certain *PT* conditions at slightly different times.

7. Discussion and geodynamic significance

The described rocks are unique in regard of a large area of accretionary prism rocks of the Western Series in the Chilean Coastal Cordillera. In particular, this concerns their unusual *PT* path, the high peak *PT* conditions, and the higher age of metamorphism and *PT* conditions. The age of the early retrograde stage of our rocks exceeds maximum ages of 250–268 Ma so far recorded for metamorphic processes in rocks of the Western Series at about the same latitude (Duhart et

al., 2001; Glodny et al., 2002a). Because the *PT* conditions of the Los Pabilos rocks are also the highest recorded so far in the Western Series, there should be a systematic relation between the highest metamorphic age, highest *PT* conditions and the counterclockwise *PT* path that demands a specific tectonic situation within the accretionary system. On the other hand, the rocks show advanced reequilibration during retrograde hydration by external fluid influx under static conditions.

Wakabayashi (1990) already provided a concise conceptional model for similar rocks in the Franciscan of California. A similar model resulted from numerical experiments presented by Gerya et al. (2002) involving the presentation of synthetic *PT* paths. These observations are consistent with the *PT* evolution in central Chile, which is summarized as a conceptual model in three steps in Fig. 10. At the initial stage of accretion, rocks are accreted to the hanging wall of the subduction channel in the deepest part of the accretionary system. Due to the proximity of the hot hanging wall, such rocks can be metamorphosed at albite-epidote-amphibolite facies conditions. They remain at depth, while the isotherms are continuously
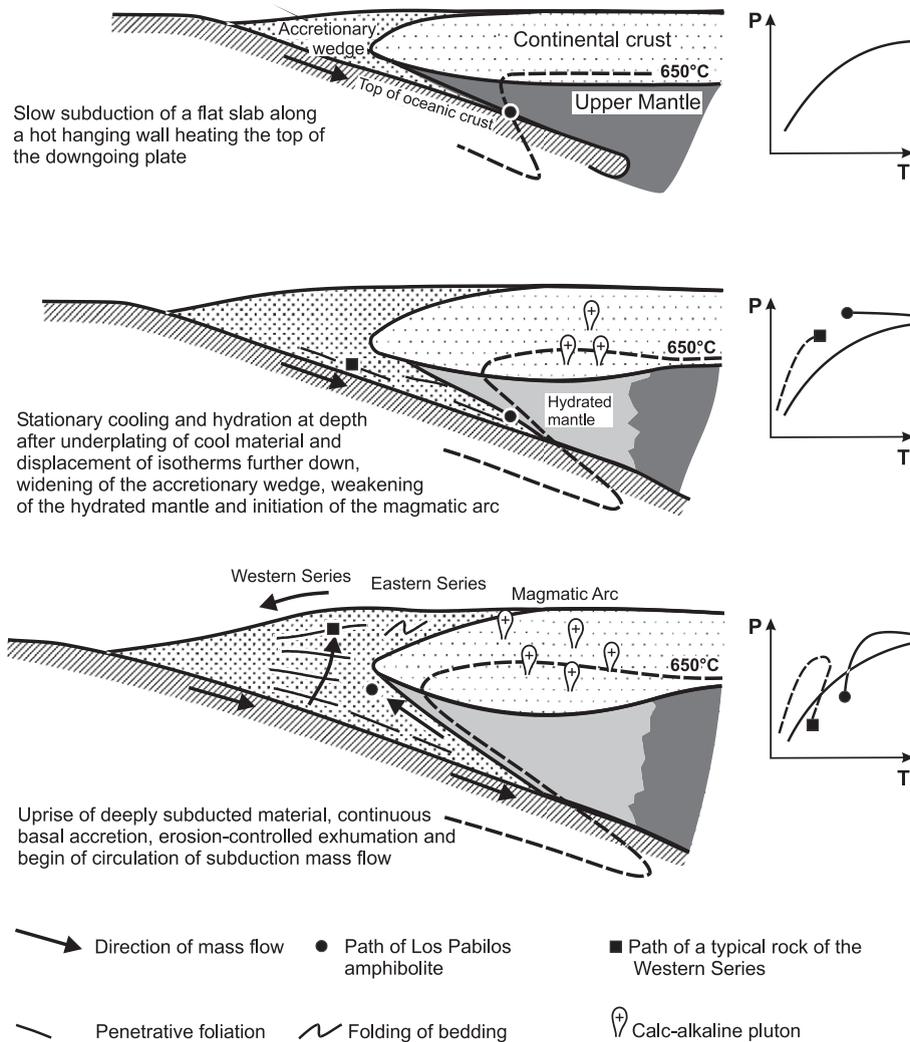

Fig. 10. Conceptual model for the early evolution of the accretionary wedge in Central Chile during the Late Carboniferous.

displaced to greater depth and the hanging wall becomes progressively cooler, hydrated and weakened. The earliest accreted rocks cool at depth contemporaneously being hydrated by infiltration of external fluids from dehydrating later subducted and accreted material. This influx is recorded by hydration of early formed assemblages and caused near-pervasive re-equilibration within these rocks, which, at a later stage, return to the surface within a cooler environment. This contrasts the behaviour of the bulk of the accreted material of the system, which rather show a continuous circulation pattern with intensive return flow from different depths and exhumation at higher temperatures compared to burial, as soon as a steady state thermal structure is built up. Such material records a normal clockwise *PT* path as is usually observed for rocks of the Western Series. Numerical modelling (Gerya et al., 2002) predicts that near-isobaric cooling during the counterclockwise *PT* evolution is dependent on the subduction rate, but in every case rather rapid (>30 °C/Ma at a subduction rate of 3 cm/year), which was in fact proved in nature by Perchuk et al. (1999). Our study did not allow a quantitative estimation of this rate, but does not exclude similar rapid cooling. However, the preserved growth zonation in garnet at the high-peak temperature reached precludes any slow cooling. The close spatial association of the garnet amphibolite of Los Pabilos with a serpentinite lens of at least 1 km length (Kato and Godoy, 1995) suggests that the serpentinite might represent a slice of the hydrated mantle in the hanging wall. Hydration and concomitant density reduction of mantle peridotites in the hanging wall of the subduction channel apparently is a rheological prerequisite for the exhumation of the early subducted material.

The garnet amphibolite of Los Pabilos is evidently not a relic of an earlier HP stage of the Western Series that has been overprinted and wiped out in most other rocks, but rather a document of the earliest stage of the subduction mass flow system in its deepest part. Considering that the isobaric cooling during this earliest stage was rapid, the derived age of 305.3 ± 3.2 Ma for the blueschist facies overprint is likely to be close to the onset of the build-up of an accretion system at the latitude considered in this study. This is in line with the age data for the onset and the main pulse of subduction-related calc-alkaline magmatism in the region (e.g. for Late Paleozoic intrusions east of Valdivia; Fig. 1):

Upper Carboniferous ages of < 316 ± 7 Ma, with most data clustering at 300–310 Ma (see Beck et al., 1991; Martin et al., 1999). Evidently, a considerable volume of metagreywackes was deeply subducted with the garnet amphibolite below the upper mantle wedge providing substantial hydrous fluids after dehydration to trigger the main volume of magmas in the arc at the earliest stage in the evolution of the paired metamorphic belt. On the other hand, Late Triassic sediments are the earliest rocks that unconformably overly this system. Hence, a continuous accretion mass flow from the Late Carboniferous until the Late Triassic seems to be plausible.

8. Conclusions

Successive overprint in garnet amphibolites suggest an anticlockwise *PT* path for a locally restricted occurrence within a fossil accretionary system. Metamorphism starts with burial in a geothermal gradient of around 15 °C/km, straddling the high-pressure part of the greenschist facies field until a transient albite-epidote amphibolite facies assemblage with coarse garnet, hornblende and epidote is reached at peak metamorphic conditions (600–760 °C, 11.0–16.5 kbar), transitional to eclogite facies (stage I) and approximately along the same gradient. This assemblage is strongly overprinted by an epidote blueschist facies assemblage at 10–14 kbar, 350–500 °C (stage II) with overgrowth of glaucophane on hornblende, titanite on rutile and partial replacement of garnet by chlorite and phengite, suggesting nearly isobaric cooling. This retrograde equilibration stage is dated with a Rb–Sr mineral isochron at 305.3 ± 3.2 Ma, somewhat younger (296.6 ± 4.7 Ma) in adjacent garnet micaschists. Growth of the blueschist assemblage involved influx of external hydrous fluids. As all matrix white mica grew during this stage, K-metasomatism might have been involved with the fluid infiltration. External fluid influx caused successive local re-equilibration and particularly local growth of chlorite and white mica continued during retrograde decompression down to ~ 300 °C and 5 kbar. The counterclockwise *PT* path contrasts the usual clockwise *PT* paths of most rocks in the accretionary system considered. The age derived for its early retrograde branch is the oldest recorded for the accretionary complex rocks at the

given latitude, whereas the peak metamorphic pressures are the highest recorded in the accretionary complex. The combination of these three characteristics appears to be a systematic feature for a tectonic scenario at the beginning of subduction mass flow in accretionary prisms worldwide, when compared with analogue examples in the literature.

Hence, we interpret our studied rocks as the earliest and deepest subducted material that was heated in contact with a still hot mantle in the hanging wall of the subduction channel. With the arrival of further accreted and subducted material that becomes progressively dehydrated, both the earliest accreted material and the mantle in the hanging wall became hydrated by external fluid influx and cooled at depth. This event is not only responsible for retrograde reequilibration, but also for a change of rheological conditions that provide effective exhumation of the early subducted material (and slices of the mantle in the hanging wall?) within a cooler environment (geothermal gradient around 10–15 °C/km) than during its burial. Summarizing, the exotic blocks of Los Pabilos provide important time markers and information about mechanisms, how subduction mass circulation was initiated in the Coastal Cordillera accretionary prism of south-central Chile. It may have started during the Late Carboniferous and lasted for nearly 100 Ma until the Late Triassic.

Acknowledgements

References

Aguirre, L., Hervé, F., Godoy, E., 1972. Distribution of metamorphic facies in Chile: an outline. Krystalinikum 9, 7–19.

Beck Jr., M.E., Garcia, A., Burmester, R.F., Munizaga, F., Hervé, F., Drake, R.E., 1991. Paleomagnetism and geochronology of late Paleozoic granitic rocks from the Lake District of southern Chile: implications for accretionary tectonics. Geology 19, 332–335.

Berman, R.G., 1988. Internally-consistent thermodynamic data for minerals in the system $Na_2O-K_2O-CaO-MgO-FeO-Fe_2O_3-Al_2O_3-SiO_2-TiO_2-H_2O-CO_2$. J. Petrol. 29, 445–522.

Berman, R.G., 1990. Mixing properties of Ca-Mg-Fe-Mn garnets. Am. Mineral. 75, 328–344.

Brandelik, A., Massonne, H.-J., 2001. New geothermobarometers on the basis of Ti incorporation into Al-garnet. 3rd EMU Workshop Solid Solutions in Silicate and Oxide Systems of Geological Importance, Lübeck 2001, Abstract, vol., 8.

Brown, T.H., Berman, R.G., Perkins, E.H., 1989. Ge0-Calc: software package for calculation and display of pressure–temperature–composition phase diagrams using an IBM or compatible personal computer. Comp. Geosci. 14, 279–289.

Dale, J., Holland, T.J.B., Powell, R., 2000. Hornblende-garnet-plagioclase thermobarometry: a natural assemblage calibration of the thermodynamics of hornblende. Contrib. Mineral. Petrol. 140, 353–362.

De Capitani, C., Brown, T.H., 1987. The computation of chemical equilibrium in complex systems containing non-ideal solid-solutions. Geochim. Cosmochim. Acta 51, 2639–2652.

Duhart, P., McDonough, M., Muñoz, J., Martin, M., Villeneuve, M., 2001. El complejo metamórfico Bahía Mansa en la cordillera de la costa del centro-sur de Chile (39°30′–42°00′S): geocronología K–Ar, 40Ar/39Ar y U–Pb e implicancias en la evolución del margen sur-occidental de Gondwana. Rev. Geol. Chile 28, 179–208.

Echtler, H., Glodny, J., Gräfe, K., Rosenau, M., Melnick, D., Seifert, W., Vietor, T., 2003. Control of inherited pre-Andean structures on neotectonics of the South-Central Andes. Abstract Lateinamerikakonferenz Freiberg. Terra Nostra 2, 27.

Evans, B.W., 1990. Phase relations of epidote-blueschists. Lithos 25, 3–23.

Forsythe, R.D., 1982. The late Paleozoic to early Mesozoic evolution of southern South America: a plate tectonic interpretation. J. Geol. Soc. (Lond.) 139, 671–682.

Gerya, T.V., Maresch, W.V., Willner, A.P., Van Reenen, D.D., Smit, C.A., 2001. Inherent gravitational instability of thickened continental crust with regionally developed low- to medium-pressure granulite facies metamorphism. Earth Planet. Sci. Lett. 190, 221–235.

Gerya, T.V., Stöckhert, B., Perchuk, A.L., 2002. Exhumation of high-pressure metamorphic rocks in a subduction channel—a numerical simulation. Tectonics 142, 6-1–6-19.

Glodny, J., Lohrmann, J., Seifert, W., Gräfe, K., Echtler, H., Figueroa, O., 2002a. Geochronological constraints on material cycling velocities, structural evolution, and exhumation of a paleo-accretionary wedge: the Bahia Mansa Complex, South Central Chile. Abstracts 5th ISAG Toulouse 2002, IRD Toulouse, pp. 259–262.

Glodny, J., Bingen, B., Austrheim, H., Molina, J.F., Rusin, A., 2002b. Precise eclogitisation ages deduced from Rb/Sr mineral systematics: The Maksyutov complex, Southern Urals, Russia. Geochim. Cosmochim. Acta 66, 1221–1235.

Glodny, J., Austrheim, H., Molina, J.F., Rusin, A., Seward, D., 2003. Rb/Sr record of fluid–rock interaction in eclogites: the Marun-Keu complex, Polar Urals, Russia. Geochim. Cosmochim. Acta 67, 4353–4371.

González-Bonorino, F., 1970. Metamorphism of the crystalline basement of central Chile. J. Petrol. 59, 979–993.

Graham, C.M., Powell, R., 1984. A garnet-hornblende geothermometer and application to the Peloma Schist, southern California. J. Metamorph. Geol. 2, 13–32.

Guinchi, C., Ricard, Y., 1999. High-pressure/low-temperature metamorphism and the dynamic of an accretionary wedge. Geophys. J. Int. 136, 620–628.

Hervé, F., 1988. Late Paleozoic subduction and accretion in Southern Chile. Episodes 11, 183–188.

Holland, T.J.B., 1980. The reaction albite = jadeite + quartz determined experimentally in the range 600–1200 °C. Am. Mineral. 65, 129–134.

Holland, T.J.B., Powell, R., 1998a. An internally consistent thermodynamic data set for phases of petrological interest. J. Metamorph. Geol. 16, 309–343.

Holland, T.J.B., Powell, R., 1998b. Mixing properties and activity–composition relationships of chlorites in the system MgO-FeO-Al$_2$O$_3$-SiO$_2$-H$_2$O. Eur. J. Mineral. 10, 395–406.

Kato, T.T., 1985. Pre-Andean orogenesis in the Coast Ranges of Central Chile. Geol. Soc. Amer. Bull. 96, 918–924.

Kato, T.T., Godoy, E., 1995. Petrogenesis and tectonic significance of Late Paleozoic coarse-crystalline blueschist and amphibolite boulders in the coastal range of Chile. Int. Geol. Rev. 37, 992–1006.

Kato, T.T., Godoy, E., McDonough, M., Duhart, P., Martin, M., Sharp, W., 1997. Un modelo preliminar de deformación transpresional mesozoica y gran desplazamiento hacia el norte de parte de la serie occidental, complejo acrecionario (38°S a 43°S), Cordillera de la Costa. Actas 8. Congr. Geol. Chil. Antofagasta 1, 98–102.

Krebs, M., Gerya, T.V., Maresch, W.V., Schertl, H.-P., Stöckhert, B., Draper, G., 2001. Serpentinite melanges of the northern Caribbean: records of complex material flow in a subduction zone, Beiheft 1. Eur. J. Mineral. 13, 104.

Kretz, R., 1983. Symbols for rock-forming minerals. Am. Mineral. 68, 277–279.

Krogh, E.I., Oh, C.W., Liou, J.G., 1994. Polyphase and anticlockwise P–T evolution for Franciscan eclogites and blueschists from Jenner, California, USA. J. Metamorph. Geol. 12, 121–134.

Martin, M.W., Kato, T.T., Rodriguez, C., Godoy, E., Duhart, P., McDonough, M., Campos, A., 1999. Evolution of the late Paleozoic accretionary complex and overlying forearc-magmatic arc, south central Chile (38°–41°S): Constraints for the tectonic setting along the southwestern margin of Gondwana. Tectonics 18, 582–605.

Maruyama, S., Liou, J.G., 1988. Petrology of Franciscan metabasites along the jadeite-glaucophane type facies series, Cazadero, California. J. Petrol. 29, 1–37.

Massonne, H.-J., 1995a. III. Rhenohercynian Foldbelt, C. Metamorphic units (Northern phyllite zone), 4. Metamorphic evolution. In: Dallmeyer, R.D., Franke, W., Weber, K. (Eds.), Pre-Permian geology of Central and Eastern Europe. Springer Verlag, Berlin-Heidelberg, pp. 132–137.

Massonne, H.-J., 1995b. Experimental and petrogenetic study of UHPM. In: Coleman, R.G., Wang, X. (Eds.), Ultrahigh Pressure Metamorphism. Cambridge Univ. Press, Cambridge, pp. 33–95.

Massonne, H.-J., 1997. An improved thermodynamic solid solution model for natural white micas and its application to the geothermobarometry of metamorphic rocks. Geol. Surv. Finland, Guide 46, Mineral equilibria and databases, Abstracts, 49.

Massonne, H.-J., Szpurka, Z., 1997. Thermodynamic properties of white micas on the basis of high-pressure experiments in the systems K$_2$O-MgO-Al$_2$O$_3$-SiO$_2$-H$_2$O and K$_2$O-FeO-Al$_2$O$_3$-SiO$_2$-H$_2$O. Lithos 41, 229–250.

Massonne, H.-J., Grosch, U., Willner, A.P., 1993. Geothermobarometrie mittels Ti-Gehalten in Kalihellglimmern. Ber. Dt. Mineral. Ges., Beih. Eur. J. Mineral. 5, 85.

Massonne, H.-J., Hervé, F., Muñoz, V., Willner, A.P., 1996. New petrological results on high-pressure, low-temperature metamorphism of the Upper Paleozoic basement of Central Chile. 3rd Int. Symp. Andean Geodynamics, St. Malo, Ext. Abstr., 783–785.

Oh, C.-W., Liou, J.G., 1990. Metamorphic evolution of two different eclogites in the Franciscan Complex, California, USA. Lithos 25, 41–53.

Parra, T., Vidal, O., Jolivet, L., 2002a. Relation between the intensity of deformation and retrogression in blueschist metapelites of Tinos Island (Greece) evidenced by chlorite-mica local equilibria. Lithos 63, 41–66.

Parra, T., Vidal, O., Agard, P., 2002b. A thermodynamic model for Fe–Mg dioctahedral K-white micas using data from phase equilibrium experiments and natural pelitic assemblages. Contrib. Mineral. Petrol. 143, 706–732.

Peacock, S., 1990. Numerical simulation of metamorphic pressure–temperature–time paths and fluid production in subduction slabs. Tectonics 9, 1197–1211.

Perchuk, A., Philippot, P., Erdmer, P., Fialin, M., 1999. Rates of thermal equilibration at the onset of subduction deduced from diffusion modeling of eclogitic garnets, Yukon-Tanana terrane, Canada. Geology 27, 531–534.

Powell, R., Holland, T.J.B., 1999. Relating formulations of the thermodynamics of mineral solid solutions: activity modeling of pyroxenes, amphiboles and micas. Am. Mineral. 84, 1–14.

Raase, P., 1974. Al and Si contents of hornblende, indicators of pressure and temperature of regional metamorphism. Contrib. Mineral. Petrol. 45, 231–236.

Smith, C.A., Sisson, V.B., Avé Lallemant, H.G., Copeland, P., 1999. Two contrasting pressure–temperature–time paths in the Villa de Cura blueschist belt, Venezuela: possible evidence for Late Cretaceous initiation of subduction in the Caribbean. Geol. Soc. Amer. Bull. 111, 831–848.

Triboulet, C., 1992. The (Na–Ca)amphibole-albite-chlorite-epidote-quartz geothermobarometer in the system S-A-F-M-C-N-H$_2$O: 1. An empirical calibration. J. Metamorph. Geol. 10, 545–556.

Vidal, O., Parra, T., 2000. Exhumation paths of high-pressure meta-pelites obtained from local equilibria for chlorite-phengite assemblages. Geol. J. 35, 139–161.

Vidal, O., Parra, T., Trotet, F., 2001. A thermodynamic model for Fe–Mg aluminous chlorite using data from phase equilibrium experiments and natural pelitic assemblages in the 100–600 °C, 1–25 kbar range. Am. J. Sci. 6, 557–592.

Villa, I.M., 1998. Isotopic closure. Terra Nova 10, 42–47.

Vinograd, V.L., 2002a. Thermodynamics of mixing and ordering in the diopside-jadeite system: I. A CVM model. Mineral. Mag. 66, 513–536.

Vinograd, V.L., 2002b. Thermodynamics of mixing and ordering in the diopside-jadeite system: II. A polynomial fit to the CVM results. Mineral. Mag. 66, 537–545.

Wakabayashi, J., 1990. Counterclockwise *PTt* paths from amphibolites, Franciscan Complex, California: relics from the early stages of subduction zone metamorphism. J. Geol. 98, 657–680.

Will, T., Okrusch, M., Schmädicke, E., Chen, G., 1998. Phase relations in the greenschist-blueschist-amphibolite-eclogite facies in the system Na_2O-CaO-FeO-MgO-Al_2O_3-SiO_2-H_2O (NCFMASH), with application to metamorphic rocks from Samos, Greece. Contrib. Mineral. Petrol. 132, 85–102.

Willner, A.P., Hervé, F., Massonne, H.-J., 2000. Mineral chemistry and pressure–temperature evolution of two contrasting high-pressure–low-temperature belts in the Chonos Archipelago, Southern Chile. J. Petrol. 41, 309–330.

Willner, A.P., Pawlig, S., Massonne, H.-J., Hervé, F., 2001. Metamorphic evolution of spessartine quartzites (coticules) in the high pressure/low temperature complex at Bahia Mansa (Coastal Cordillera of Southern Central Chile). Can. Mineral. 39, 1547–1569.